

QUANTITATIVE BIOLOGICAL STUDIES
AT CELLULAR AND SUB-CELLULAR LEVEL

A dissertation
presented to
the faculty of the Graduate School
at the University of Missouri-Columbia

In Partial Fulfillment
of the Requirements for the Degree
Doctor of Philosophy

By

BASARAB GABRIEL HOSU

Dr. Gabor Forgacs, dissertation supervisor

MAY 2007

The undersigned, appointed by the dean of the Graduate School, have examined the dissertation entitled

**QUANTITATIVE BIOLOGICAL STUDIES
AT CELLULAR AND SUB-CELLULAR LEVEL**

presented by Basarab Gabriel Hosu,

a candidate for the degree of doctor of philosophy,

and hereby certify that, in their opinion, it is worthy of acceptance.

Professor Gabor Forgacs

Professor David Worcester

Professor Anand Chandrasekar

Professor Ioan Kosztin

Professor Paul Miceli

ACKNOWLEDGEMENTS

I would like to thank my advisor, Dr Gabor Forgacs for creating a cross-disciplinary environment in his lab which allowed people with different backgrounds to express and interact freely. I would also like to thank my committee members for helping me to make this dissertation better and providing me with valuable feedback from their fields of expertise. I am grateful to my collaborators for sharing with me their knowledge and teaming us up in challenging projects. I would like to thank my teachers, professors, labmates and administrative staff in both Biology and Physics Departments for their precious help during my graduate student years.

I would like to thank my wife for her love and support, my parents and my (now) toddler son for bringing joy to my life.

TABLE OF CONTENTS

ACKNOWLEDGEMENTS	iii
LIST OF FIGURES	vii
LIST OF TABLES	ix
ABSTRACT	x
Chapter	
1. INTRODUCTION	1
2. MAGNETIC TWEEZERS FOR STUDIES IN THE LIFE SCIENCES	3
Definition and background	3
Design particularities	6
Development	10
The sample holder	10
Magnetic pulse/camera exposure timing	11
Computer interface	13
XY microscope stage monitoring	19
Data analysis	20
Calibration	25
Problems to deal with	25
Procedure	27
Measuring the properties of the magnetic field	27

Determining the magnetic properties of the beads	29
Determining the exact location of the area of interest	34
When to recalibrate	37
3. MAGNETIC TWEEZERS APPLICATIONS	38
Applications at cellular level	40
Membrane tether formation study.....	40
Background and significance	40
Specific aims	42
Experimental design.....	43
Results.....	46
Discussion	55
Crooks fluctuation theorem verification at cellular level	58
Background and significance	58
Specific aims.....	61
Experimental design.....	63
Results.....	65
Conclusion	72
Applications at sub-cellular level.....	75
Background and significance	75
Specific aims	78
Experimental design.....	78
Oocyte collection and bead injection	78
Experimental group assignment.....	78
Magnetic tweezers experiments.....	80
Modeling and data analysis.....	81

Proof of concept on somatic cells	84
Results.....	85
Magnetic bead movement through the intracellular environment.....	85
Effect of cryopreservation on intracellular viscoelastic properties	89
Effect of LatA pretreatment on intracellular viscoelastic properties in thawed oocytes	89
Effect of LatA pretreatment on somatic cell cryopreservation	89
Discussion.....	91
References.....	95
Vita	105

LIST OF FIGURES

Figure	Page
1. Magnetic tweezers workstation.....	7
2. Schematic representation of the measuring unit of the magnetic tweezers.	8
3. Magnetic tweezers block diagram.....	14
4. Magnetic tweezers control application (1).....	16
5. Generating current waveforms.....	17
6. Magnetic tweezers control application (2).....	18
7. Magnetic force calculator.....	23
8. Drift/noise removal.	24
9. Induced magnetization as measured by SQUID.	30
10. Magnetic force determination through Stokes law.	32
11. Magnetic moment of the bead as determined through the calibration process.	35
12. Overall verification of the calibration process through Stokes law.....	36
13. Schematic illustration of extracting a membrane tether by magnetic tweezers.....	47
14. Typical time-displacement curves in membrane tether pulling experiments.....	48
15. Membrane tethers: optical microscopy.....	49

16. Membrane tethers: field emission scanning electron microscopy (FESEM).	50
17. Voigt model for multiple tether formation.....	53
18. Estimating the total number of tethers.	54
19. FR method to calculate the potential of mean forces.....	62
20. Experimental design for Crooks fluctuation theorem verification.	67
21. Force profile and typical displacement curve for two switching (1 and 4 s) times between two given force values.....	68
22. Force-displacement curves for the experiment depicted in Fig. 21.....	69
23. The variation of free energy associated with the tether pulling process, as determined through the FR method.....	70
24. Force profile and typical bead displacement for reconstruction of free energy profiles.	71
25. Free energy profile vs. tether length (n = 14 experiments).....	68
26. CD-1 mouse oocyte injected with a 5-micron paramagnetic bead.	79
27. Viscoelastic model for the cytoplasmic environment.	82
28. Typical bead trajectory under a 2-second constant force pulse.	86
29. Results: viscoelastic parameters in all experimental groups.....	87
30. Proof of concept in somatic cells.	90

LIST OF TABLES

Table	Page
1. Summary of the quantitative results obtained in membrane tether study.....	55
2. Quantitative results in oocyte cytoskeleton study.....	88

ABSTRACT

A magnetic tweezers is a device capable of exerting force of controlled amplitude on biological structures through transducers, typically paramagnetic beads. The first part of this dissertation describes in detail the development of a translational magnetic tweezers setup capable of generating both constant force pulses and complex force patterns of controlled amplitude in the range of 1-1000 pN over distances of hundreds of microns. The second part describes the biological applications that powered the magnetic tweezers development: quantitative biomechanical studies at cellular (extracellular) and sub-cellular (intracellular) level.

The **extracellular** studies addressed the process of membrane tether formation in eukaryotic cells. Tethers are nanotubular structures, which can be extracted out of the cell membrane by applying localized forces. We used the magnetic tweezers to extract simultaneously multiple tethers under constant force transduced to cells through magnetic beads attached to their membranes. The tethers were visualized by optical and scanning electron microscopy and quantitatively characterized in terms of membrane viscosity, elasticity and relaxation time. The contribution of the actin cytoskeletal network in the process of tether formation was also investigated. An interesting extension of this project focused on the verification of the Crooks fluctuation theorem (a fundamental recent

finding in non-equilibrium thermodynamics) at the mesoscopic (i.e. membrane tether) level.

The **intracellular** studies involved the measurement of cytoplasmic viscoelastic coefficients of mouse oocytes using magnetic beads trapped into their cytoskeletal mesh. The motivation for this work was to improve on the success of oocyte cryopreservation, in particular on cryosurvival rate, by preserving the developmental competence of the eggs. We started out by quantifying the changes in the biophysical properties of the oocyte cytoskeleton induced by cryopreservation and found that cryopreservation altered all the viscoelastic parameters measurable with the tweezers. This finding inspired the hypothesis that the reversible disassembly of the actin cytoskeleton prior to cryopreservation prevents it from being damaged uncontrollably during freezing. We evaluated the effect of latrunculin A pretreatment on cryopreserved oocytes by using the viscoelastic parameters as markers of cytoskeletal integrity. The results showed that the relative number of oocytes that survived cryopreservation was higher in the latrunculin pretreated group. Moreover, the viscoelastic parameters in latrunculin treated survivors were similar to those of fresh oocytes. This finding promoted latrunculin A as a candidate drug for improving both cryosurvival and developmental competence in oocytes. The reversible dismantling of the actin cytoskeleton represents, conceptually, a novel approach to cryopreservation. The concept was also tested on somatic cells.

1. INTRODUCTION

The magnetic tweezers was pioneered in 1949 [1] by Francis Crick. Thirteen years before being awarded with a Nobel Prize for his discovery concerning the molecular structure of nucleic acids, he was trying to determine the viscoelastic parameters of the cytoplasmic environment of living cells by displacing magnetic particles trapped into their bodies. Despite its' over 58 years of documented existence and unlike complementary techniques such as optical tweezers (OT) or atomic force microscopy (AFM), magnetic tweezers are not yet widely commercially available. Specific applications require specific constructions, hence the huge variety of designs reported in literature.

As the magnetic tweezers delivers its force through magnetic fields, it reaches regions inaccessible by other methods: the intracellular environment. Although primarily designed to explore the interior of the cell, the magnetic tweezers has also proven to be an excellent tool for quantitative measurements in the extracellular environment, competing directly with OTs and AFM. Our particular construction allows generating constant forces over distances as long as 500 μm , exceeding from this point of view the capabilities of the mentioned techniques (limited in both OT and AFMs by the maximum displacement of the piezoelectric actuator, to tens of microns).

Carrying out my PhD work in a cross-disciplinary laboratory, I had the chance to get involved in developing both the instrument and its biological applications. My thesis

reflects both aspects. The first part of my dissertation describes in detail the magnetic tweezers design and development. The second part details the two biological applications, at cellular (membrane tether formation study) and sub-cellular (cytoskeletal study) level. Both projects evolved beyond their original goal. The study on membrane tether formation started by observing a biological phenomenon and progressed by suggesting a biophysical model to quantify the biological observations. Eventually, the tether system was used as a model to test the Crooks fluctuation theorem (a fundamental recent discovery for systems far from equilibrium) at the cellular level. The intracellular study started with the characterization of the cytoskeletal network of mouse oocytes and ended up by discovering a new cryoprotective agent, whose applicability was verified in somatic cells as well (a finding that constitutes the material of a patent application in process).

Developing the biological applications required adjustments and redesigning of the instrumentation for new capabilities. Each new development created new experimental opportunities. This aspect, probably fairly common in research but not always obvious in the typical paper one reads in a journal, continuously supplied my enthusiasm. I have tried to capture this in my writing.

2. MAGNETIC TWEEZERS FOR STUDIES IN THE LIFE SCIENCES

Definition and background

A magnetic tweezers is a device capable of exerting torque or force of controlled magnitude and direction on magnetic particles. In fewer words, it is a magnet.

To be biologically relevant, the torque or force is applied to a specific biological structure, such as a biomolecule or a cellular component (i.e. plasma membrane, cytoskeleton) through a transducer. Typically, a transducer is a bead of appropriate size containing a paramagnetic core (usually Fe_3O_4 or a combination of Fe_2O_3 and Fe_3O_4) coated with a biocompatible polymer. The bead is attached to the specific biological structures and subjected to magnetic torque or force. Whether the tweezers is rotational (torque-producing) or translational (force-producing) it can be applied to both intra- and extracellular studies. In a typical application a super-paramagnetic particle is magnetized and subsequently rotated or translated. The rotation or trajectory of the moving particle is recorded to gain insight into the biophysical properties of its surrounding environment. Rotational magnetic tweezers [2-5], by their very nature can explore only a small region of space, whereas translational ones are capable of providing information on a larger scale.

Magnetic tweezers presently in use differ greatly in their design and capabilities. To bring about the magnetic effect they use either permanent magnets or electro-magnets. They are employed either to carry out quantitative measurements on a particular biological structure or to micromanipulate a target structure.

Magnetic tweezers based on permanent magnets have the advantage of being simple. They do not require external power and do not generate heat. On the other hand, the magnetic field cannot be easily varied or turned on/off quickly. They have been used for both single-molecule measurements [2, 6, 7] and viscoelastic measurements in living cells [8-10].

Electromagnet-based tweezers are more popular. They range from simple-coil designs [11-15] to complex constructions with two [16], four [17, 18], six [19] or eight [20] coils. Single-coil magnetic tweezers have been used for micromanipulation [14], single-molecule measurements [15], as well as extracellular [12, 13] or intracellular [11] viscoelastic measurements on living cells.

Though simple, single-coil magnetic tweezers have a serious limitation: they are not able to generate a constant spatial magnetic gradient over a decent (cell size) area. Since the magnitude of the magnetic force in a spatially varying field depends on the magnetic field's gradient, single-coil devices cannot exert a constant magnetic force on a moving magnetic particle. This disadvantage prevents consistent measurements from being carried out, especially when the displacement of the particle is considerable. Thus, multiple-coil designs are preferred when having a constant spatial magnetic gradient is important [16, 17]. Some multi-coil constructions [19, 21] are intended for complex

three-dimensional micromanipulations. In these designs, the objective is to rapidly change the direction of the force, rather than maintain a constant force.

An important aspect in designing a reliable translational magnetic tweezers is its capability of “saturating” the bead’s magnetic material. Besides the gradient, the force exerted on a magnetic particle depends on its magnetic moment:

$$\vec{F}_M = \vec{\nabla}(\vec{m} \cdot \vec{B}) = \vec{\nabla}(mB) \quad (1)$$

The magnetic moment, m , in turn, depends on the magnetization of the bead’s material:

$$m = MV \quad (2)$$

Here M and V are respectively the magnetization and volume of the particle. When a paramagnetic particle is placed in a magnetic field, the magnetic moment it develops depends on the strength of the field. However, upon increasing the field strength, the magnetic moment eventually stops increasing. It saturates. If in the region of interest B is large enough so that M reaches its saturation value, furthermore $B_y = 0$ and $B_z = \text{constant}$, then eq. (1) reduces to:

$$F_y = VM_x \frac{\partial B_x}{\partial y} \quad (3)$$

Equation (3) forms the basis of our in house developed translational magnetic tweezers operation. Thus, to generate a constant force on a moving particle, not only the

spatial magnetic gradient over the area of motion must be constant, but also the magnetization of the particle ought to remain unchanged. As a consequence, in a spatially varying field the only way to keep the magnetization constant is to magnetize the material to saturation. Some designs accomplish this goal by using two sets of coils: a pair to generate a constant magnetic field, which magnetizes the particle to saturation and a second pair to generate the magnetic gradient [17].

Design particularities

The original design tried to meet the following specifications:

1. Provide a high constant magnetic gradient over typical cellular dimensions (tens to hundreds of microns), capable of generating forces strong enough to displace beads trapped inside cells.
2. Provide a strong enough magnetic field capable of magnetizing superparamagnetic beads to saturation.
3. Generate both continuous magnetic fields and magnetic pulses.
4. Have a sufficiently compact size to fit onto the stage of an inverted microscope without interfering with the microscope's functionality.

The apparatus consists of two coils with a very specific pole profile (measuring unit) and an adjustable constant current source (control unit). The measuring unit is mounted on the stage of an Olympus IX-70 inverted microscope and connected to the control unit (see Figs. 1 and 2).

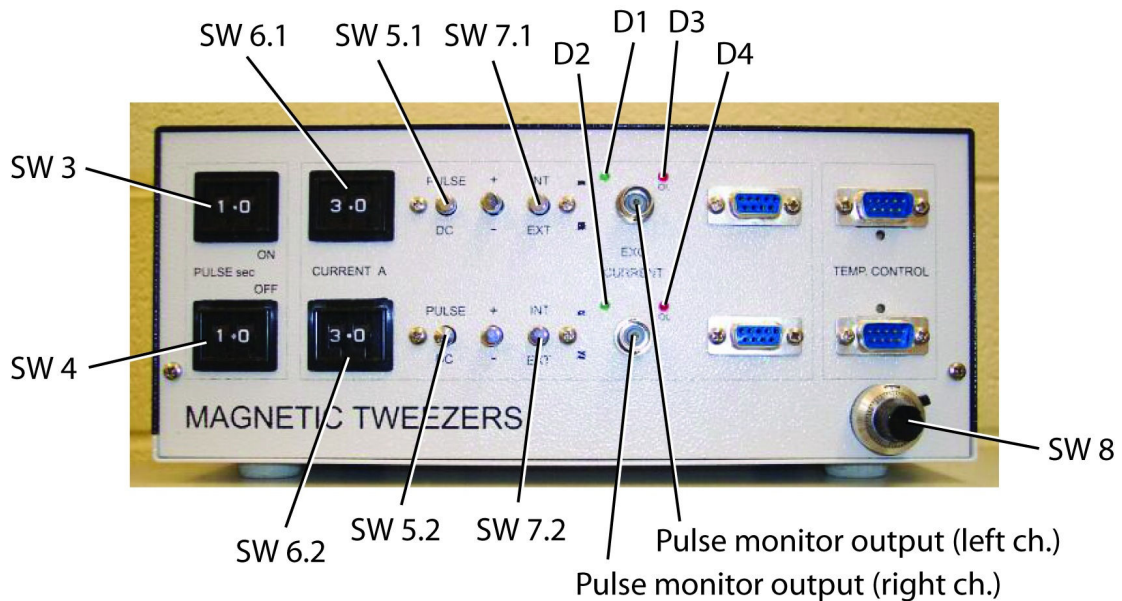
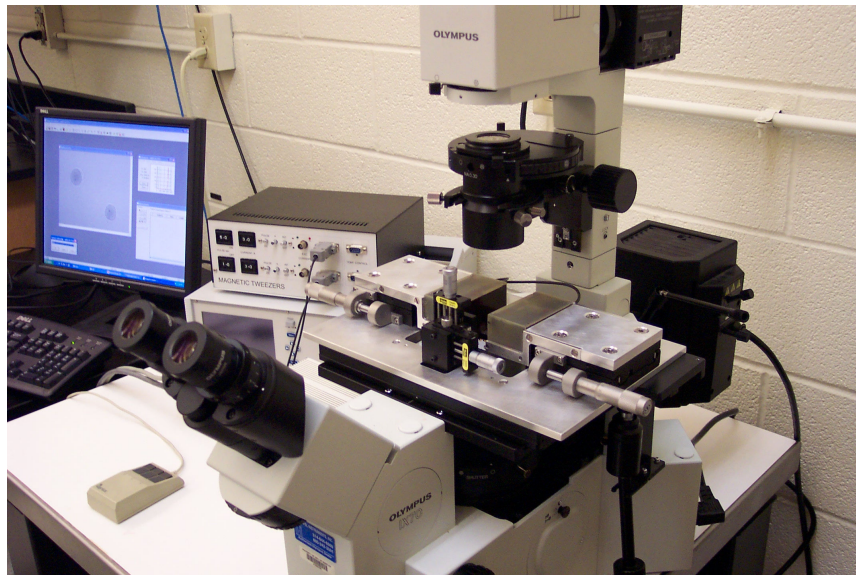


Figure 1. Magnetic tweezers workstation.

Upper panel. General view of the magnetic tweezers workstation. The two coils of the measuring unit are mounted on the microscope stage. The sample holder can be slightly moved up/down and left/right with a bidirectional micromanipulator (visible between the two coils). The mouse-like device triggers the magnetic pulse. *Lower panel.* Front panel of the magnetic tweezers control unit. The 4 dials on the left (SW 3, SW 4, SW 6.1 and SW 6.2) adjust the length of the pulse and the time between pulses in 0.1 sec increments, as well as the amplitude of the current through the coils in 0.1 A increments. Internal/external switches (SW 7.1 and SW 7.2) allow the magnetic pulses to be controlled by an external source. Labels refer to the block diagram in Fig. 3.

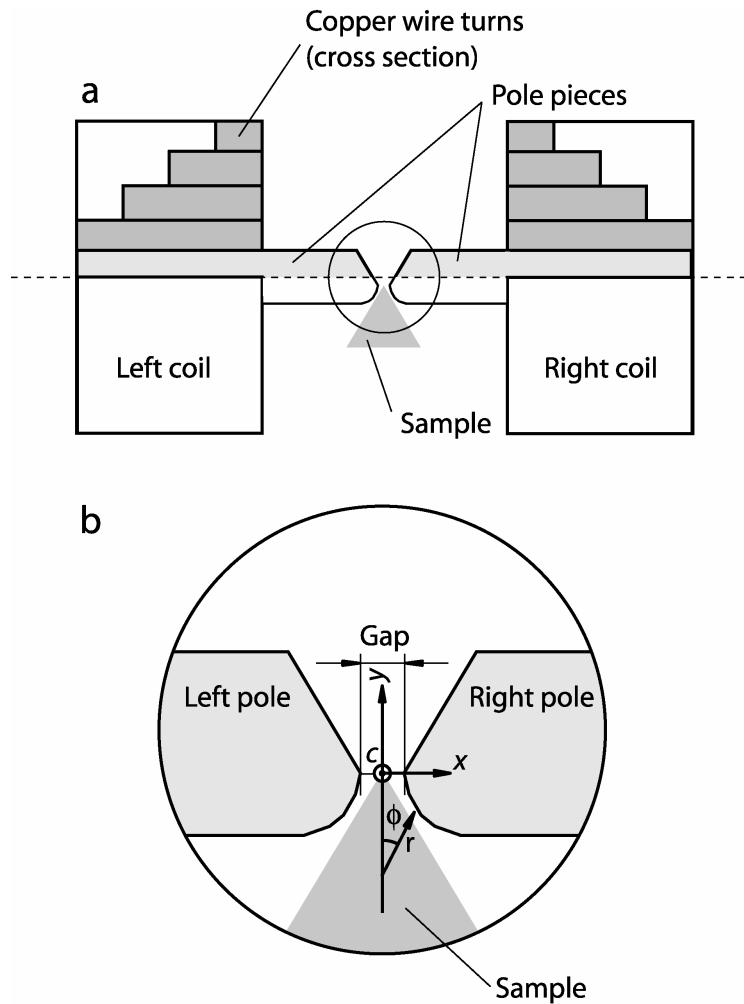


Figure 2. Schematic representation of the measuring unit of the magnetic tweezers.

Upper panel. Top view. The special coil structure is symmetric with respect to the broken line; details below the broken line are not shown. *Lower panel.* Details of the pole piece profile; C , the central point (also referred as “point C ”), serves as origin of the two-dimensional coordinate system. The shaded triangle represents the shape and location of the sample holder.

The special profile of the pole pieces assures a constant magnetic gradient over extended regions and $B_y = 0$ along the midline (y direction) as well as a small (virtually negligible) variation of B_z on z between the poles. The constant magnetic gradient is larger in the lower (curved) region, which is machined according to the equation:

$$r^{3/2} \sin(3\phi / 2) = \text{const.} \quad (4)$$

(for notations, see Fig. 2) [22].

The two coils are used to simultaneously magnetize the magnetic particles and create a constant magnetic gradient along the y direction (for details see [16]). This makes the tweezers compact and its positioning on the stage of an inverted microscope convenient, as there is no need for extra magnetizing coils.

The original design allowed the apparatus to be used in both continuous and pulse modes. In the former case a magnetic particle can be translated for long enough time to explore the entire intracellular environment or considerable regions of the extracellular milieu. In the pulse mode, the particle can be moved and stopped intermittently for desired time periods.

Output data (bead displacement under magnetic force) is acquired by video microscopy through a CoolSNAP_{fx} digital video camera (Photometrics, Tucson, AZ) in Image Pro Express (IPE, Media Cybernetics, San Diego, CA).

Development

Making the magnetic tweezers functional in a biological context required a series of modifications of the original design described above. As particular applications emerged, new capabilities have been added to the device.

The sample holder

The first important development addressed the sample holder. One of the most important components of the magnetic tweezers setup, the sample holder serves to place the biological sample (living cells with super-paramagnetic beads attached or embedded) in between the two magnetic poles, in conditions as close as possible to the ones used in a normal cell culture environment (cell culture medium). In addition, the cytoskeletal experiments carried out on single oocytes required that the sample holder be easily accessible and not hinder the oocyte micromanipulation, carried out with glass micropipettes.

After trying several constructions, the successful design turned out to be a removable stage, which can easily be mounted and un-mounted from its working location between the magnetic poles. The removable stage, secured in working position through non-magnetic thumb screws, accommodates a triangular coverslip which protrudes in between the magnetic poles (see the triangular shaded area in Fig. 2). The triangular coverslip is made by cutting rectangular coverslips with a diamond scribe. Depending on its size, the triangular coverslip can accommodate up to 200 μ l of culture medium which forms a convex meniscus on its surface, covering the cells. Evaporation during the experiments tends to reduce the amount of culture medium and concentrate the solutes in the remaining liquid. Adding more medium at the beginning of the experiment alleviates

the problem, but alters the optics (the meniscus becomes more pronounced), making the bead tracking more difficult. Tests performed in the experimental conditions (room temperature) showed that evaporation can be neglected in experiments lasting shorter than ~20 minutes (the evaporation rate is ~0.9 $\mu\text{l}/\text{min}$). The evaporation rate increases with temperature; working at 37 °C requires replacing the triangular coverslip with a triangular prismoidal shaped chamber capable of accommodating more liquid. The triangular shape of the coverslip allows the sample to reach in the space between the magnetic poles while preventing the poles to get in contact with the coverslip or the liquid above, eliminating thus the medium leaking and the effect of magnetostriction (physical motion of the pole pieces when turning the magnetic field on).

In case of membrane tether experiments, the cells are directly cultured on the triangular coverslips, in Petri dishes. Right before an experiment, the coverslips are removed from the dishes and glued to the removable stage of the sample holder with grease. In case of oocyte experiments, a clean coverslip is first glued to the removable stage and covered with liquid which will be later gelled. A single oocyte is then plunged into the liquid with a glass micropipette (under a dissection microscope) and placed in a convenient location (as close as possible to the tip of the coverslip along the y axis of the tweezers). After triggering the gelation of the liquid (see the next chapter for details), the sample holder is mounted in its working position.

Magnetic pulse/camera exposure timing

In its original design, the magnetic tweezers generates magnetic pulses of controllable length and amplitude. The bead motion is captured by a digital video camera

mounted on the optical side port of the microscope. While the image acquiring parameters (the exposure time and the time between frames, but some other parameters as well) are controlled through the commercially available software Image Pro Express (IPE), the magnetic pulse parameters are set up directly through dials on the front panel of the control unit of the magnetic tweezers (Fig 1). Both processes (image acquisition and magnetic pulse generation) are triggered manually. The output of an experiment is the bead trajectory, i.e. its xy location in each frame with respect to a reference frame.

In order to eventually plot a time-displacement curve of the bead during the experiment, each frame has to be time-stamped. As IPE does not provide a time stamp on the acquired images but triggers the camera according to precise input parameters, the first thought was to rely on the “time between exposures” setting in its menu. For instance, an exposure time of 10 ms combined with a time between exposures of 90 ms results in 100 ms between two consecutive frames, a value which can be inferred for the whole sequence of frames. Preliminary tests showed that, even though the exposure time was accurately controlled by IPE, the time between exposures was not. When set up at low values (around 100 ms or below), the real time between exposures could be any number between the desired one and ~250 ms (in most instances higher). The “culprit” turned to be the camera itself. According to the manufacturer, the camera transfers each image to the computer right after it has been taken. If the following frame is set up to be taken after an interval shorter than the transfer time, then it is simply delayed without notice. In turn, the transfer time depends on the complexity (size) of the image to be transferred. Therefore, the “time between exposures” parameter is not reliable and does not offer any clue about its real value (at least in the range of interest of 10-100 ms). The

solution was to time stamp each frame through a Labview application which analyzes digital signals provided by the camera while acquiring the images.

Since the magnetic pulse and the video acquisition are not synchronized, the pulse can start within any video frame or anywhere between any two consecutive frames. In the experiments intended to determine the viscoelastic parameters, the data analysis requires analyzing the creep, i.e. the bead trajectory during a step pulse, starting from the very moment the pulse is applied. This moment, which does not necessarily correspond to a camera frame, has to be somehow time stamped, and used as “0” reference in the subsequent fitting. The time stamping of the pulse is also carried out in Labview, using a digital signal obtained by passing the analog output monitoring signal from the tweezers (0.01-0.4 V) through a Schmidt trigger (see Fig. 3) set up to switch at around 0.01 V (corresponding to a current of 0.1 A through the coils).

Computer interface

In the experiments designed to verify the Crooks fluctuation theorem at mesoscale level, the force is varied according to various patterns during the acquisition, within a single experiment. Succession of force steps, ramps and plateaus are applied to the sample. To accomplish this with our constant force magnetic tweezers, the current through the coils has to be changed accordingly. Adding this capability required making the tweezers completely computer controllable. We opted for an economical solution built around a relatively inexpensive digital input/output National Instruments board (see the magnetic tweezers block diagram in Fig. 3).

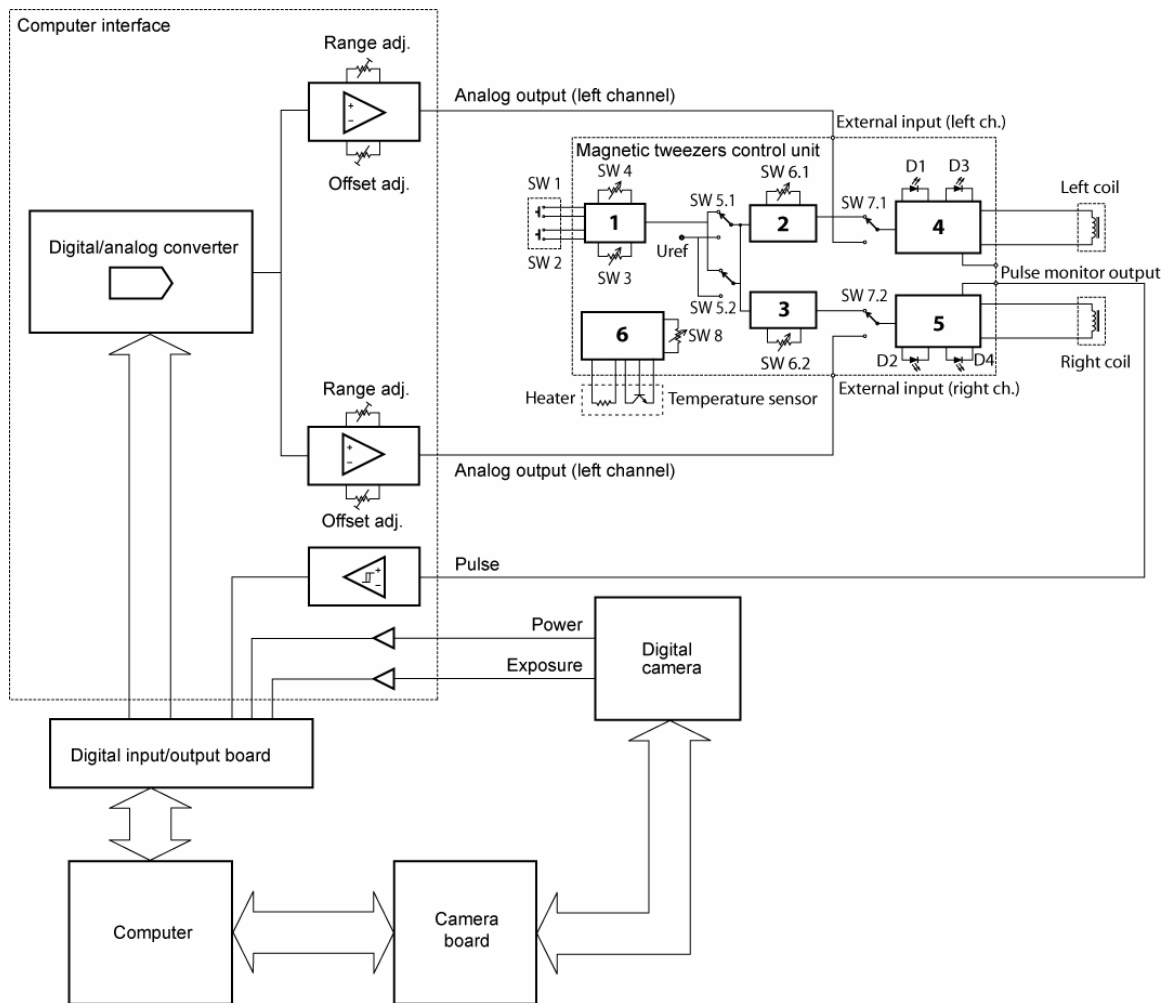


Figure 3. Magnetic tweezers block diagram.

The magnetic tweezers control unit (upper right, part of the original design, see also the front panel in Fig. 1) is composed by an adjustable pulse generator (1) triggered by the external switch SW 1. SW 3 and SW 4 adjust the length of the pulse and the interval between pulses, respectively. SW 2 (located on a mouse-like device together with SW 1 for convenient operation) forces the output of the pulse generator in DC mode. The signal from (1) is amplified by two preamplifiers (2) and (3), one for each channel (coil), and supplied to voltage/current converters (4) and (5) which, in turn, supply the two coils of the measuring unit. SW 6.1 and SW 6.2 adjust the gain of the preamplifiers and are scaled on the front panel directly in A (0.1 to 3 A). D1-D4 are LEDs which monitor the pulse (D1 and D2) and overloads (D3, D4). Pulse monitor outputs from (4) and (5) allow measuring directly the current through each coil with an external volt-meter (current/voltage rate 0.1 V/1 A) and also provide feedback for the computer interface. SW 5.1 and SW 5.2 force the tweezers in DC mode. SW 7.1 and SW 7.2 allow connecting the voltage/current converters (4) and (5) to the computer interface which overrides the internal pulse management (see the text for details).

The digital outputs of the NI I/O board are connected to a digital to analog converter which feeds the voltage/current converters from the magnetic tweezers control unit through buffer amplifiers. The buffer amplifiers have offset and range adjustments. The inputs read digital signals coming from (1) the video camera (a signal which confirms that the camera is powered on and one which is “high” during exposure, used for time stamping) and from (2) the tweezers control unit (the output of the Schmidt trigger used to time stamp the magnetic pulse). The electronics was built from scratch using active components offered as free samples by National Semiconductors and Texas Instruments. The operation of the magnetic tweezers is controlled by a Labview application (see Fig. 4) which carries out the following tasks:

1. Synthesizes the desired force waveform (see also Fig. 5).
2. Sends the waveform to the computer interface board.
3. Monitors the camera exposure and the magnetic pulse during the experiment and records their status in a text file, which will be used by a tracking program for time stamping.

While the Crooks fluctuation theorem application evolved, more complicated force waveforms were required. To increase the versatility, the force waveform synthesis component was removed from the magnetic tweezers control application and developed as a stand alone application capable of synthesizing more complex waves. The synthesized waves are saved as intermediary files and loaded as necessary by the tweezers control application before the experiment (see Fig. 6).

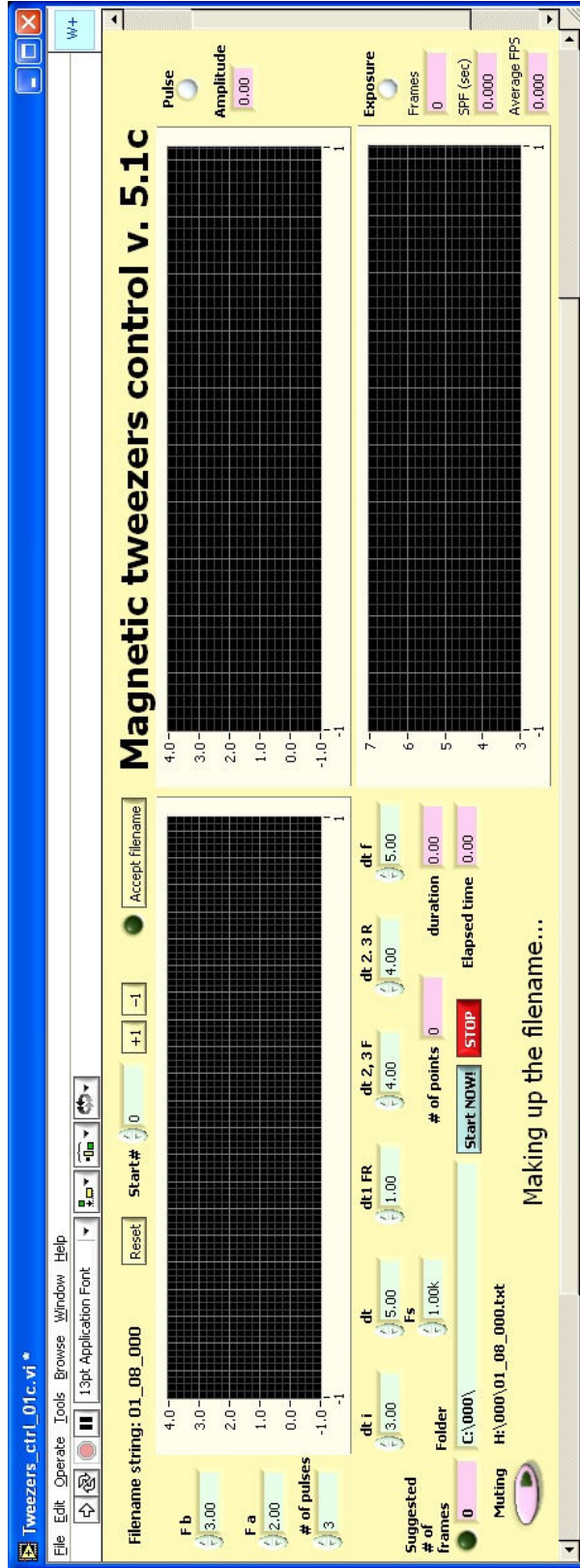


Figure 4. Magnetic tweezers control application (1).

This Labview program generates different current patterns (successions of steps, ramps and plateaus, see also Fig. 5) and applies them to the magnetic tweezers coils. It also records in a file the camera exposure data and the pattern of the current during the experiment, allowing the bead tracking software to time stamp the bead trajectory. The left chart displays the generated current pattern. The upper right chart displays the instantaneous value of the current through the coils. The lower right chart indicates status of the camera (displays a pulse each time the camera exposes).

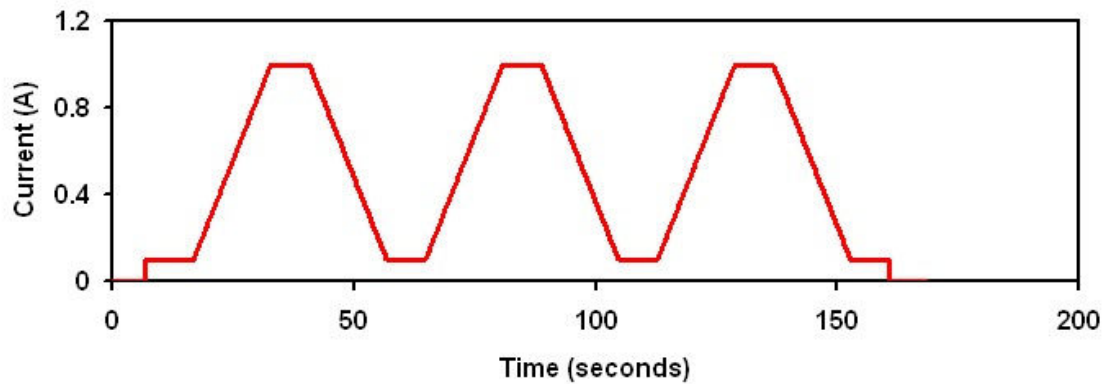
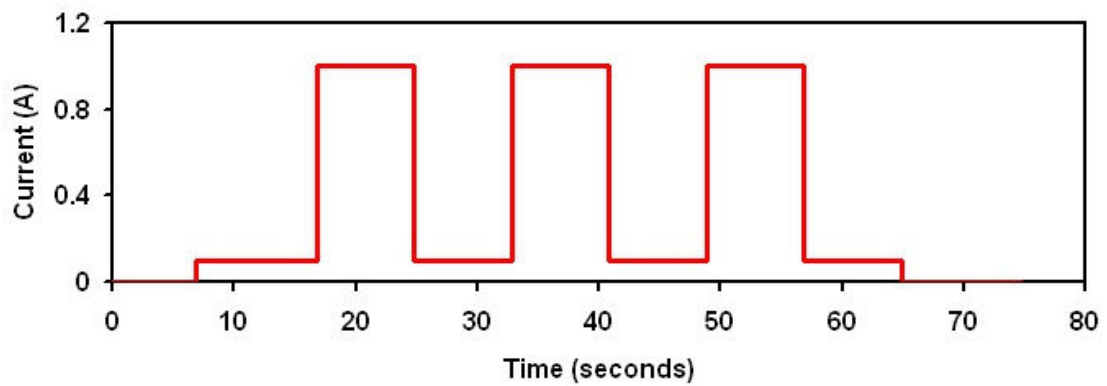
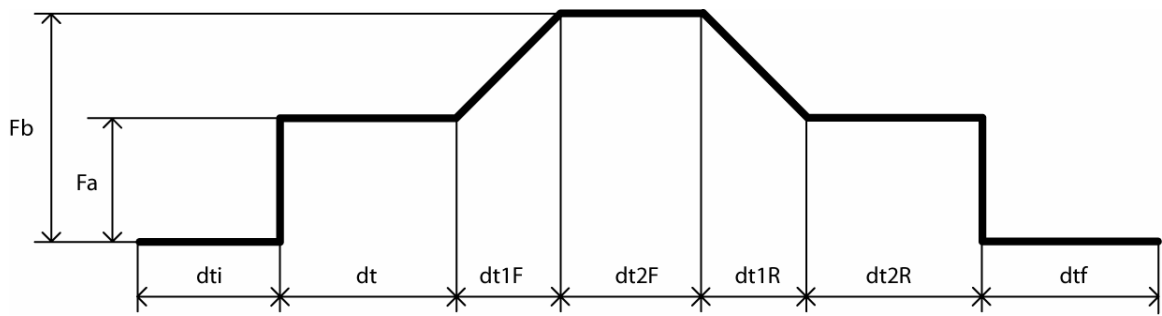


Figure 5. Generating current waveforms.

Upper panel. Basic current pattern generated by the application in Fig. 4. *Middle panel.* Example of current pattern generated in an actual experiment. The control parameters have the following values: $F_a = 0.1$ A; $F_b = 1$ A; $dt_i = 7$ s; $dt = 10$ s; $dt_{1F} = dt_{1R} = 0$ s; $dt_{2F} = dt_{2R} = 8$ s; $dt_f = 10$ s; # of pulses: 3. *Lower panel.* Example of current pattern generated in an actual experiment. The control parameters have the following values: $F_a = 0.1$ A; $F_b = 1$ A; $dt_i = 7$ s; $dt = 10$ s; $dt_{1F} = dt_{1R} = 0$ s; $dt_{2F} = dt_{2R} = 8$ s; $dt_f = 10$ s; # of pulses: 3.

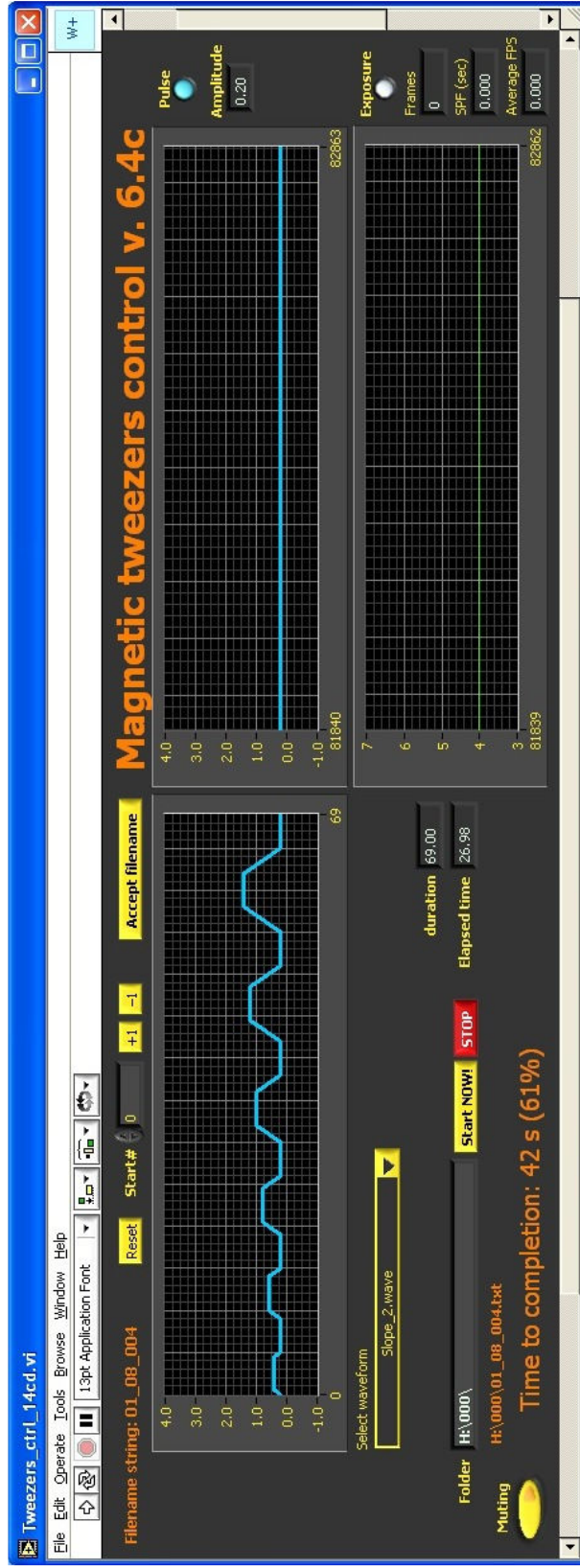


Figure 6. Magnetic tweezers control application (2).

This Labview program, a simplified version of the one presented in Fig. 4, loads a waveform (pattern of current, “Slope_2_wave” here, plotted in the graph on the left) from a pre-generated pool and applies it to the magnetic tweezers coils. Generating the waveform with a dedicated application (not shown here) allows more complex waveform to be created and increases the versatility of magnetic tweezers control application.

XY microscope stage monitoring

The segment of the entire y axis suitable for experiments is as long as 7,500 μm . Most of our experiments were carried out at distances $> 3,000 \mu\text{m}$ from the central point, some of them as far as 7,000 μm from the central point. In these regions, depending on the value of the current used in the experiment, the beads might not be magnetized to saturation. The gradient, constant for at least 200 μm at any location (up to 500 μm in certain locations) is different between remote locations. As mentioned below, the magnetic induction along the y axis could be well fit with a double exponential. This exponential curve can be approximated by a succession of contiguous straight segments of at least 200 μm , in which the gradient can be considered constant. However, the values of the gradient (i.e., the slopes of the straight segments) are different from segment to segment, which is what makes all the calibration measurements along the y axis (described below) necessary.

Determining the value of the force in a given experiment requires the xy coordinates of the area of interest (the region on the coverslip where the measurement is carried out) with respect to the magnetic poles. As both the magnetic poles and the sample holder are mounted rigidly on the microscope stage, the xy coordinates of the field of view can be determined by monitoring the motion of the microscope stage. This was accomplished by using a commercially available 800 dpi optical mouse mounted on the body of the microscope. The mouse monitors the xy displacement of an optical pattern on a pad which moves together with the microscope stage. This economical solution provides the xy coordinates in increments of $\sim 32 \mu\text{m}$. The force calibration

measurements showed that the magnetic force does not change significantly with the distance for at least 200 μm along the y axis, a value over 6 times larger than the accuracy of this stage tracking system. The mouse signal is processed by a Labview application which displays directly on the computer screen the X and Y values of the center of the field of view with respect to the reference. The application also provides visual and acoustical “over range” alarms when the field reaches locations where measurement should not be attempted (for instance, where no force calibration data is available). It also allows recalibrating the system for optical sensors (mice) with different resolutions.

Data analysis

The output of each experiment consists of two files: (1) a image sequence file, generated by IPE (technically a multi-page uncompressed tif file, where each page represents a frame) and (2) a text file generated by the magnetic tweezers control application which contains the (a) information necessary to time stamp the frames, (b) the magnetic pulse, as well as (c) the waveform of the magnetic current through the coils. The two files are analyzed by set of Labview programs, as follows:

1. A “sequence reader” program, which converts the multi-page tif file into three-dimensional numeric arrays. Each array has a certain number of pages (corresponding to the number of frames in the video sequence), each page being an xy pixel map of the respective frame (an array of numbers, each number representing the brightness of the corresponding pixel).
2. A particle tracking program, which: (a) detects the advancing and the trailing edge of the bead on the vertical (V) and horizontal (H) directions and examines

successive frames to determine the edge displacement; (b) time stamps each frame based on the information contained in the text file generated by the magnetic tweezers control application during the experiment; (c) time stamps the magnetic pulse: if the magnetic pulse started, ended or the current through the coils (and implicitly, the magnetic force) changed its value in between two frames, it introduces “virtual” frames (extra time points) at the moment of change. The output of the tracking program is composed of two files, each containing (1) the position of the bead in each frame projected on the V or H direction, (2) the time stamp and (3) the value of the current (one file for V and one file for H). The tracking program does not make any assumption concerning the shape of the tracked particle. It can track particles of any shape, provided the shape does not change during the experiment.

3. A “composer” program which analyzes the V and H files created by the tracking program, detects the overall direction of movement of the bead and plots the bead position vs. time along that direction. It also plots the XY displacement of the bead.

4. A “force calculator” program (see Fig. 7), which replaces the values of the current through the coils with the corresponding values of the force, based on the information provided by the XY microscope stage monitoring program and a reference calibration file created during the calibration process (see details below, under “Calibration”).

5. Occasionally, we also used a “drift remover” program, to improve on the accuracy of the bead tracking. We initially created this program for the cytoskeleton measurements on oocytes. The initial goal was to subtract the motion of the whole oocyte from the total displacement of the bead, to deal with some rare instances in which the

experiment was initiated before the liquid surrounding the oocyte was completely gelled (see more details in next chapter). It turned out that the program was also useful for removing unwanted drift noise present in almost any measurement, such as the (very small) drift of the microscope stage during the experiment and some strange periodic noise on V direction (which we strongly suspect came from the fan which cools the Peltier element of the CoolSNAP_{fx} camera CCD). For an example of drift/noise removal process, see Fig. 8.

The drift removal solution is particularly useful in instances where the bead displacement is small (generally the drift is below 0.3 μm , therefore it would pass unnoticeably in cases of bead displacements of tens of microns). To have use of the drift removal program, one first needs to track the drift itself. In case of oocyte experiments, this implies tracking the displacement of the edge of the cell. In case of membrane tether experiments, the edge of the cell (which is flat, attached to the substrate) is less pronounced, therefore more difficult to track. Besides, it can change during longer experiment (cells can move on the substrate). In such instances, latex beads attached to the substrate can be used to monitor the drift, or even magnetic beads strongly attached to the glass substrate (according to our experience, once a magnetic bead attaches to the glass substrate, it will never detach, regardless how big the applied magnetic force is).

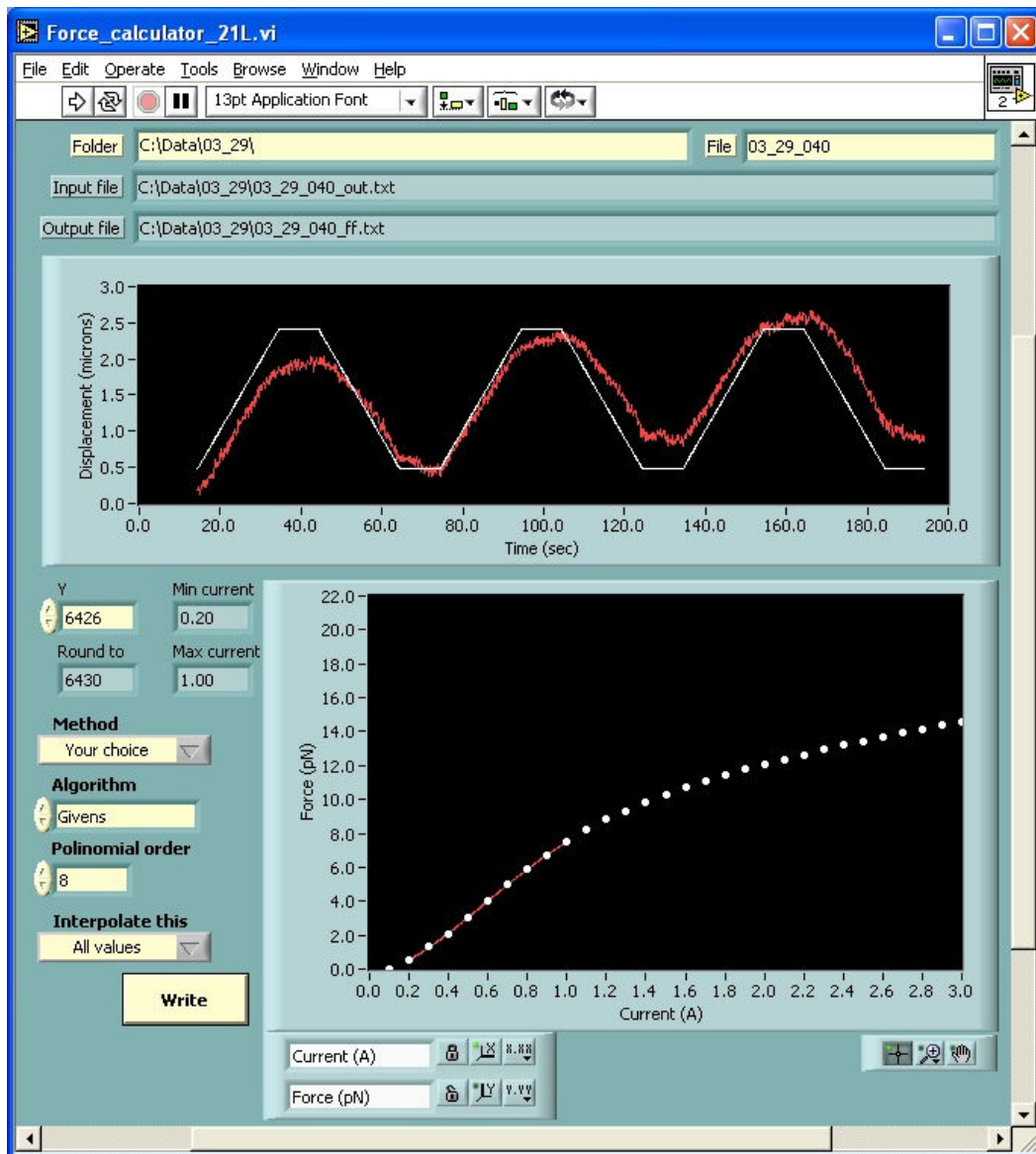


Figure 7. Magnetic force calculator.

To calculate the force acting on the bead, this Labview program takes into account the distance of the area of interest from point C (in Fig. 2), along the y axis (“Y”, 6,426 μm here), as well as a reference chart prepared through the calibration process (see under “Calibration”). The upper graph displays the trajectory of the bead in the experiment (the red line) and the profile of the current through the coils (the white line). The lower graph shows the corresponding values of the force for certain values of the current, as obtained from the reference chart (the white filled circles) and the interpolated values for the particular values used in this experiment (multiple values along the red line). The “Write” button, when pressed, replaces the values of the current in the input file with the corresponding values of the force.

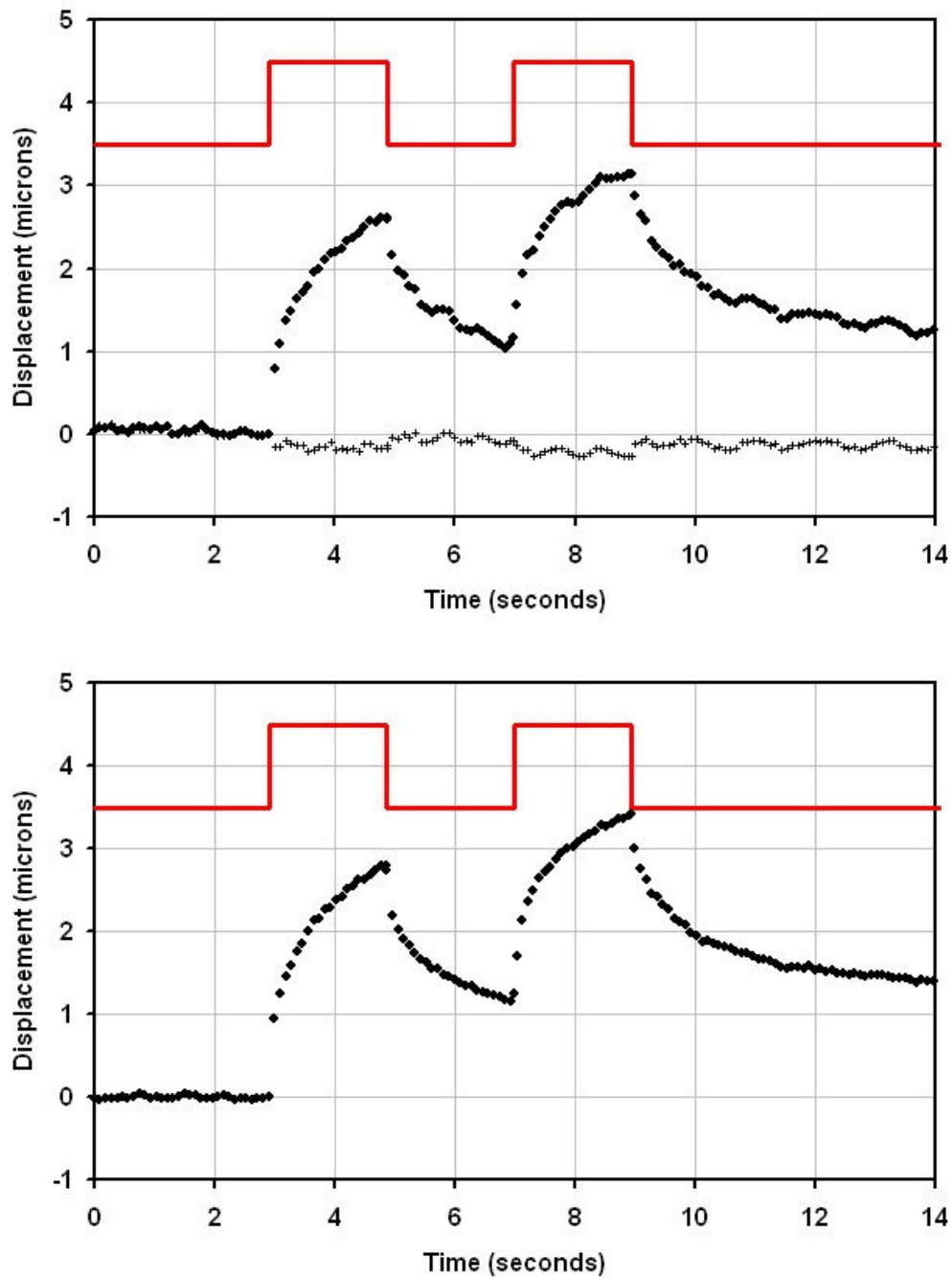


Figure 8. Drift/noise removal.

Magnetic bead trajectory in a mouse oocyte under two 2-second magnetic pulses. *Upper panel.* Solid circles: bead trajectory before drift/noise removal; Crosses: drift/noise, as determined by tracking the edge of the cell. Solid line: magnetic pulse. *Lower panel.* Bead trajectory after subtracting the drift/noise.

Calibration

Calibration refers to a series of procedures employed to determine the magnetic force acting on the bead in a given experiment. In the current setup, the magnetic force represents the independent variable (the control parameter). The biological response is assessed by analyzing the bead displacement (the dependent variable) under given force. Meaningful quantitative measurements can only be carried out if the force acting on the bead at any time is precisely known.

Problems to deal with

In theory, the magnetic force only depends on the parameters of the magnetic field (magnetic induction and gradient) and the characteristics of the bead (dimension and magnetic properties), see equations (1)-(3) above. Ideally, the beads are identical and always magnetized to saturation. Therefore, the force acting on each of them is only proportional to the magnetic gradient. In turn, thanks to our Faraday balance design, the gradient is constant over a long distance along the y axis and can be directly measured with a Hall probe connected to a Gauss-meter. Therefore, the calibration procedure is expected to be a straight forward process, if the bead characteristics are known. One only needs to measure the gradient and calculate the force as in equation (3).

Complementarily, Stokes law allows the direct determination of the magnetic force without any magnetic field measurement, by moving the bead in liquids with known viscosity, as described in ref. [16].

In reality, the situation was more and the calibration was one of the most difficult problems we encountered in the magnetic tweezers development. The main issues that made the calibration process difficult were the followings:

1. The calibration procedure is carried out on beads different from the ones used in the actual experiments. Individual bead micromanipulation is difficult and requires expensive equipment. Even if the individual micromanipulations were trivial, chances to recover the bead after a successful experiment and use it *a posteriori* to determine the force acting on it in the experimental conditions are very slim. In case of intracellular experiments, at the end of an experiment the bead is trapped inside the cell which, in turn (as described later), is embedded in a fibrin gel. In case of extracellular experiments, the bead, if still attached to the cell, is connected to it through very fragile structures (membrane tubes with diameters of tens of nanometers), very easy to break. Therefore, the calibration procedure should characterize as precisely as possible a batch of beads, rather than individual beads. Selecting the most homogeneous batches available on the market is also a key issue.

2. Within a batch, the beads are not identical as far as their size and magnetic content are concerned. Manufacturers do not explicitly recommend their beads for single bead measurements (most if not all commercially available beads are rather designed for magnetic separation of biological materials, which is a qualitative process; in this case, the exact value of the magnetic force acting on each bead is not really important). Two similar, but not identical, beads placed under identical magnetic conditions (induction, gradient) might transduce two different forces.

3. Sometimes measurements are carried out in regions where the beads are not magnetized to saturation. This happens when the area of interest is far away from the two poles, along the y axis. In a real experiment, the exact location of the cell with respect to the poles (i.e. its location along the y axis) is not easily controlled (see details below, in the applications chapter). In the current setup, y axis is as long as 7,500 microns. Even though the magnetic gradient is constant over hundreds of microns (see ref [16]), the absolute value of the magnetic induction drops at one point below the saturation level. If the cell is located in a region where the magnetic induction is below the saturation level, the magnetization of the bead has to be calculated, based on the magnetic properties of the beads. Unfortunately, these properties are not always easily available, some manufacturers being reluctant to disclose them.

Calculating the exact magnetic force acting on beads requires the following information:

1. The properties of the magnetic field (magnetic induction and magnetic gradient) along the y axis;
2. The magnetic properties of the beads (magnetic susceptibility, saturation curve) for the batch of beads used in an experiment;
3. The exact location of the area of interest in a given experiment.

Procedure

Measuring the properties of the magnetic field

The magnetic induction along the y axis can be measured directly with a Hall probe connected to a Gauss-meter. We used a model STF71-0204-05-T Hall probe (the

smallest probe available at the time of acquiring the instrument) and an FW Bell Model 7010 Gauss meter (both from Bell Technologies, Orlando, FL). All measurements were carried out for a gap of 500 microns between the magnetic poles. The magnetic induction was measured for 7,500 μm along the y axis, starting from the central point between the poles (the closest point between the poles, “C” in Fig. 2), by displacing the Hall probe in 100-micron increments with a micromanipulator. In each spatial point, the measurement was carried out for currents ranging between 0.1 A and 3.0 A in 0.1 A increments. The central point of the magnetic tweezers was matched with the central point of the Hall sensor by slightly displacing the Hall probe in xyz directions while checking the Gauss-meter for the maximum reading.

The results of the magnetic induction measurements were written in a chart with 76 rows (each row corresponding to a certain distance from the central point along the y axis, from 0 to 7,500 μm in 100-micron increments) and 30 columns (each column corresponding to a given current, from 0.1 to 3.0 A, in 0.1 A increments).

The magnetic induction chart was used to calculate a corresponding 75×30 magnetic gradient chart. In order to generate a continuous gradient chart based on the discrete magnetic induction measurements, the data for each current was fit with double exponentials in Labview. All subsequent calculations were based on the fit values.

The limitations of this method relate the size of the Hall sensor (physical dimensions: 0.5 mm thickness, 3 mm width, with active sensor dimensions: 2.7 mm height and 2 mm width), with the following consequences:

a. The magnetic induction measurements are not possible for gaps between poles smaller than 500 μm at distances closer than 2,000 μm to the central point (there is no physical room for the probe) and, more importantly,

b. The field measurements are not reliable between 0 and 1,000 μm (half the width of the active sensor) along the y axis, (“0” being the central point between the poles). By concept, the Hall probe measures the average magnetic induction across its active sensor area ($2 \times 2.7 \text{ mm}$). Due to the geometry of the pole profiles, the magnetic induction is maximal in the central point and decreases monotonically along the y axis, in both directions. As the edge of the active area of the Hall sensor reaches and then passes the central point (assuming that the Hall probe is moved along the y axis towards the central point), the average value displayed on the Gauss-meter screen starts comprising field values from the other side of the central point, where the magnetic induction decreases again. This results in incorrect readings for magnetic induction in instances where the active sensor of the probe reaches on the other side of the central point (above point “C” in Fig. 2). Consequently, magnetic induction measurements in these areas were not taken into account when calculating the magnetic force.

Determining the magnetic properties of the beads

The magnetic induction chart prepared as described above is used to calculate a **bead magnetization chart** (the magnetization of the bead for a given location along the y axis and a given current through the coils). Such a calculation requires knowing the magnetization curve of the beads (bead magnetization vs. magnetic induction). In turn, the bead magnetization chart is used in connection with the **magnetic gradient chart** to calculate (by employing equation (3)) the **magnetic force chart** (magnetic force vs.

current through the coils for different locations along the y axis), which represents the final output of the calibration process.

One way to obtain the magnetic properties of the beads is by contacting the manufacturer. If manufacturer data is not available, the magnetization of the beads can be measured directly or indirectly.

The direct method relies on a superconducting quantum interference device (SQUID). We used this method to determine the magnetization of 1.28 micron super-paramagnetic beads in [16] (see Fig. 9). Once the magnetization of the bead under a given magnetic induction is known, the magnetic force chart can be easily calculated.

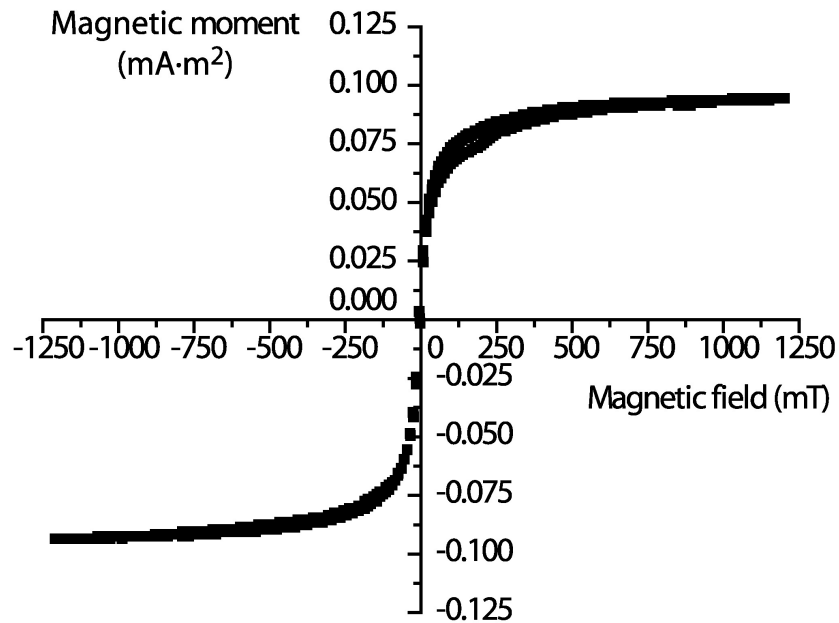


Figure 9. Induced magnetization as measured by SQUID.

The apparatus measured the total induced moment of a 20 μl suspension of 1.28 micron beads with concentration 5.5×10^{10} beads/ml. From this the average saturation magnetic moment of a single bead is $m = 7.26 \times 10^{-14}$ A·m² and the saturation magnetization of the bead's material is $M = 6.6 \times 10^4$ A·m.

An alternative, indirect way to determine the magnetic properties of the beads, which does not require a SQUID is through the Stokes law. We used this method to calibrate the magnetic tweezers force for the 5 micron super-paramagnetic beads used in the membrane tether and cytoskeletal measurements. The magnetic force acting on a magnetic bead moving in a fluid is counterbalanced by the viscous force given by the Stokes formula, thus

$$F_M = 6\pi\eta r v \quad (5)$$

where η , r and v are respectively the viscosity of the fluid, the radius of the bead and its velocity (see Fig. 10).

To calculate the magnetization chart for the 5 micron beads we used the following protocol:

1. Determine the magnetic force (F_M) acting on a bead for a current through the coils of 1 A, along the entire y axis. This step required moving one single (same) bead for 7,500 μm through a viscosity standard liquid, while measuring the bead velocity. The output is a chart of F_M vs. distance (y) for one current value (1 A).

2. Determine the magnetic moment of the bead as a function of distance (y). This was accomplished by plugging the magnetic gradient values for the corresponding current (1 A) and distance (y) (from the magnetic gradient chart prepared as described above) in the equation:

$$m = \frac{F_M}{\frac{\partial B_x(y)}{\partial y}} \quad (6)$$

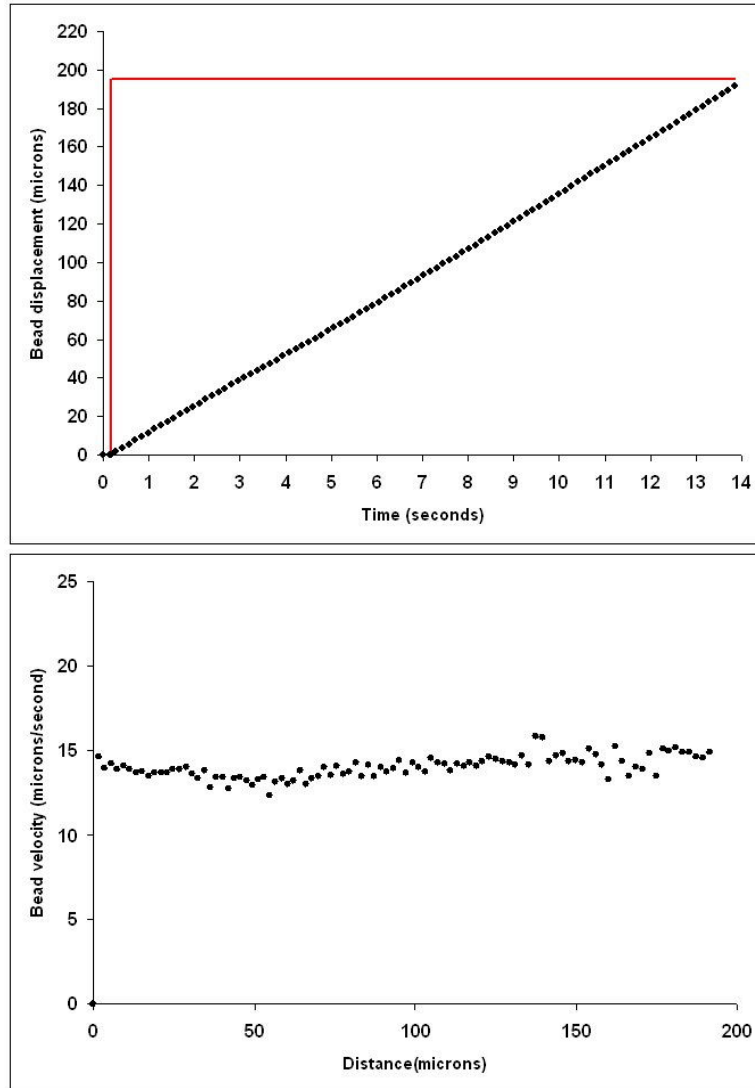


Figure 10. Magnetic force determination through Stokes law.

Upper panel. Bead trajectory (solid circles) under a force step (solid line). *Lower panel.* Instantaneous bead velocity as determined by plotting the numerical first derivative of the trajectory in upper panel. The bead velocity is constant ($\sim 15 \mu\text{m/s}$) during the entire 200 micron displacement, demonstrating that the force acting on it is constant.

In order to generate the continuous function of $m(y)$, similarly to the case of the magnetic gradient, the discrete values of m were fit to an exponential. All subsequent calculations were based on the fit values.

3. Create a chart of the **magnetic moment vs. y** , by using (a) the chart prepared at pct. 2 (m vs. y) and (b) the **magnetic induction vs. y** chart available from the magnetic field direct measurements. This chart provides directly the magnetic moment of the bead for a given magnetic induction.

4. Finally, create a chart F_M vs. y for all values of the current (0.1 to 3.0 A).

All charts and calculations were created and carried out in Microsoft Excel. All fittings were performed in Labview. The final chart (magnetic force vs. y for currents ranging from 0.1 to 3.0 A in 0.1 A increments) was saved as a text file and used as calibration reference data for the Labview program which calculates the force value for currents in between increments, by interpolation (see Fig. 7, above). Basically, the program reads the file generated by the tracking program (which comprises (a) the timestamp of each frame along with (b) the corresponding position of the bead and (c) the value of the current through the coils) and replaces the values of the current with the corresponding values for force. If the exact values of the current do not appear in the calibration reference file (which only contains current values in 0.1 increments, the white filled circles in the lower graph in Fig. 7), the corresponding force is calculated by interpolation with an 8th order polynomial fit through a Givens algorithm (red line in the lower graph in Fig. 7).

Determining the exact location of the area of interest

Determining the precise values of the force along the y axis through a laborious calibration process only makes sense if the exact location of the area of interest (where the experiment is carried out) is known (see above, under “XY microscope stage monitoring”). The size of the field of view in the experimental conditions (CoolSNAP_{fx} camera and 20x objective) is about $438 \times 347 \mu\text{m}$. Stacked one on top of another, there are > 21 fields of view along the 7,500 micron y axis. The magnetic poles are never visible in the field of view, thus the distance to them cannot be directly (or reliably) estimated. For this reason, we developed a hardware/software solution which permanently monitors the distance (xy coordinates) of the center of the field of view with respect to the central point between the poles. The coordinates (particularly y) should be recorded before (or after) each experiment. Force measurements carried out by employing Stokes law showed that the force does not vary significantly across the x axis [16]. Failing to record the coordinates renders the quantification impossible, thus the experiment useless.

Fig. 11 shows the magnetic properties of 5-micron magnetic beads as determined through the calibration process described above. Fig. 12 depicts an overall verification of the calibration process carried out by moving a 5-micron magnetic beads under a force profile similar to the ones used in Crooks fluctuation theorem application.

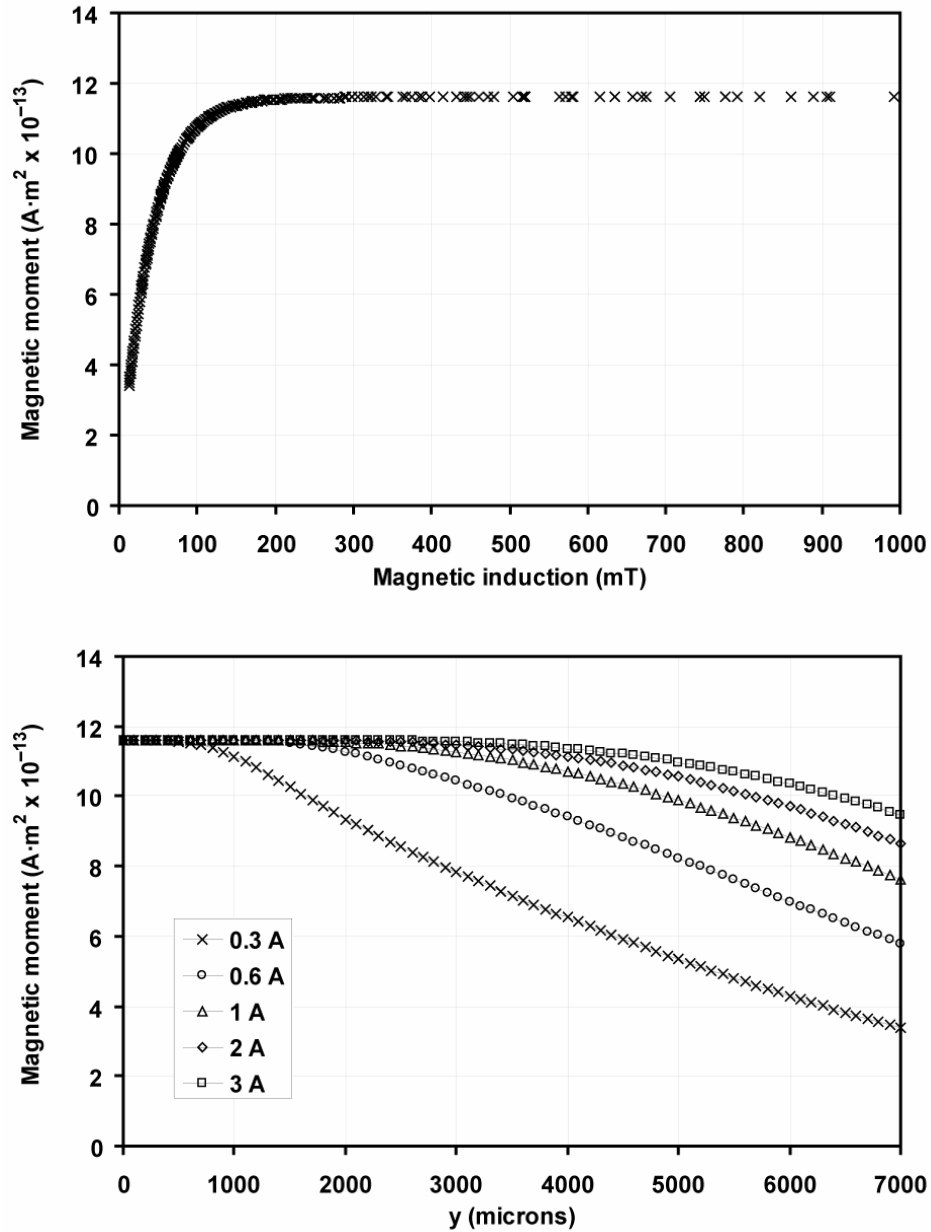


Figure 11. Magnetic moment of the bead as determined through the calibration process.

Upper panel. Magnetic moment of the bead as a function of magnetic induction. The saturation magnetization of the bead material was found to be $7.4 \times 10^4 \text{ A}\cdot\text{m}$ (a bit higher than the value of $6.6 \times 10^4 \text{ A}\cdot\text{m}$ determined for the 1.28 micron magnetic beads by SQUID, reported in [16]). *Lower panel.* Magnetic moment of the bead at different locations between the poles along the y axis for different currents through the coils.

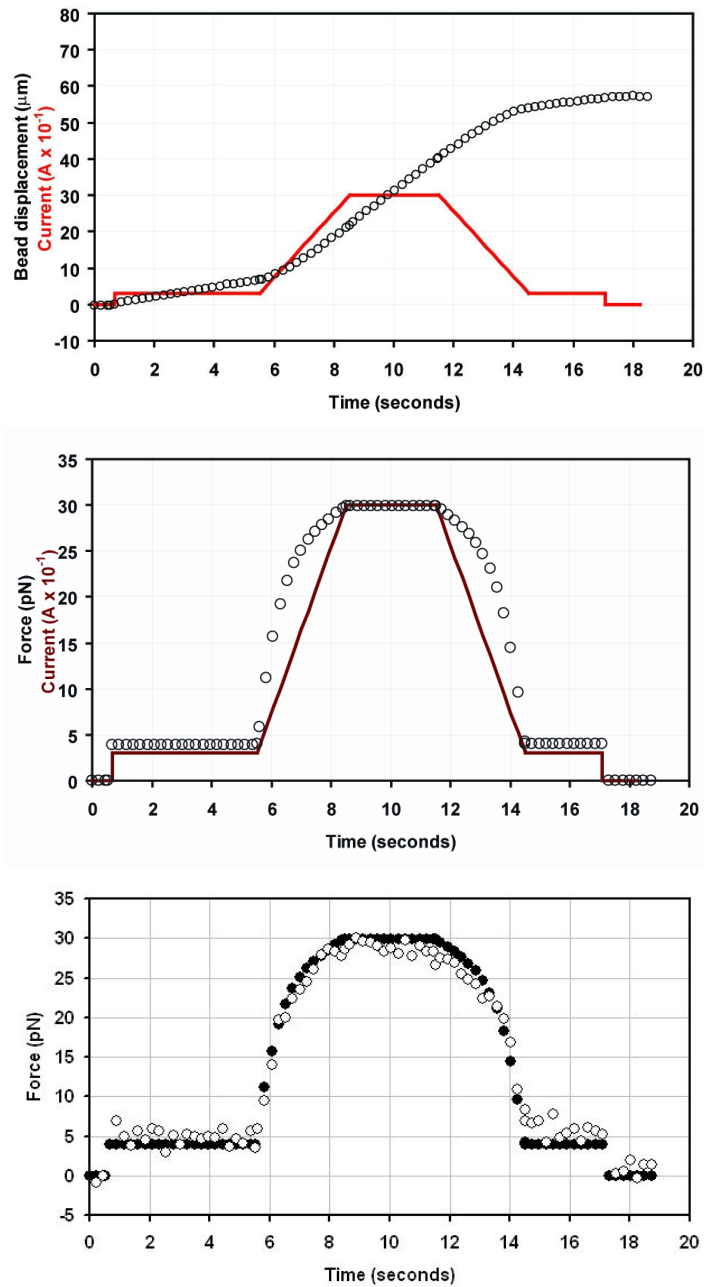


Figure 12. Overall verification of the calibration process through Stokes law.

Upper panel. Magnetic bead trajectory (open circles) during a specific force profile. The solid line represents the profile of the current through the coils of the magnetic tweezers. *Middle panel.* The force values (open circles) corresponding to the current profile shown in the upper panel (solid line). *Lower panel.* Magnetic force acting on the bead while applying the force profile showed in the middle panel as calculated from the instantaneous bead velocity in upper panel (open circles) and as expected from the calibration process (solid circles).

When to recalibrate

Changing the magnetic beads (size, manufacturer, maybe even batch) requires repeating partially the calibration (only the second part, “Determining the magnetic properties of the beads”, since the properties of the magnetic field only depend on the geometry of the poles). Changing the distance between the magnetic poles (to anything else than 500 microns) requires repeating all the field measurements, but not the magnetic moment measurements. In any case, the recalibration eventually leads to a new reference file for the Labview program (no change in program is necessary).

3. MAGNETIC TWEEZERS APPLICATIONS

The main (a better word, which takes into account the evolution of the original projects, might be “departing”) scientific interest of our lab is biomechanics at various levels: cellular, sub-cellular and supra-cellular (tissue). The two main applications which powered the magnetic tweezers development addressed the first two levels: **cellular** (also referred below as **extracellular**) and **sub-cellular** (also denoted as **intracellular**; extra- and intracellular refer to the location of the bead with respect to the cell).

The **cellular studies** addressed the process of membrane tether formation in eukaryotic cells. Tethers are nanotubular structures, which can be extracted out of the cell membrane by applying localized external or internal forces. Physiologically, they form for example in the process of leukocyte rolling or metastatic cell movement along vascular walls and are used to anchor the cells to prepare for extravasation. Tether nanotubes play important role also in intracellular and cell-to-cell communication. We used the magnetic tweezers to extract simultaneously multiple tethers under constant force transduced to cells through magnetic beads attached to the cell membrane. We visualized the tethers by optical and scanning electron microscopy and quantitatively characterized them in terms of membrane viscosity, elasticity and relaxation time. We also investigated the contribution of actin cytoskeletal network in the process of tether formation.

An interesting extension of this project focused on the verification of the Crooks fluctuation theorem (a fundamental recent finding in non-equilibrium thermodynamics) at the mesoscopic (i.e. membrane tether) level, as opposed to its recent demonstration at molecular level ([23]). This work was carried out in collaboration with Dr. Ioan Kosztin's group from the Physics Department at UMC.

The **intracellular** studies involved the measurement of cytoplasmic viscoelasticity of mouse oocytes using magnetic beads injected into the cells. The motivation for this work (performed in collaboration with Dr. John Critser's group from the College of Veterinary Medicine, UMC) was to improve on the success of oocyte cryopreservation, in particular on cryosurvival rate, by preserving the developmental competence of the cells. We started out by quantifying the changes in the biophysical properties of the oocyte cytoskeleton induced by cryopreservation and found that cryopreservation altered all the viscoelastic parameters. This finding generated the hypothesis that the reversible disassembly of the actin cytoskeleton prior to cryopreservation prevents it from being damaged uncontrollably during freezing. We evaluated the effect of Latrunculin A (LatA) pretreatment on cryopreserved oocytes by using the viscoelastic parameters as markers of cytoskeletal integrity. The results showed that the relative number of oocytes that survived cryopreservation was higher in the LatA pretreated group. The viscoelastic parameters in LatA pretreated survivors were similar to those of fresh oocytes. Concurrent fertilization experiments carried out in Dr. Critser's lab, showed that LatA pretreatment induced a nearly twofold increase in the number of oocytes that reached the blastocyst stage. The joint work demonstrated that cytoskeletal integrity, as assessed by viscoelasticity measurements, can be used to assess the

efficiency of the cryopreservation procedure and promoted LatA as a candidate drug for improving both cryosurvival and developmental competence in oocytes. The reversible dismantling of the actin cytoskeleton represents, conceptually, a novel approach to cryopreservation. To prove this concept, we also tested it on somatic cells. This provided the basis of a provisional patent application we filled with UMC.

Applications at cellular level

Membrane tether formation study

Background and significance

Membrane tethers have been described as nanotubular protrusions from the surface of phospholipid bilayers. They are involved in numerous cellular processes, such as: (a) leukocyte attachment to the endothelial wall [24-26] prior to extravasation; (b) metastatic spreading of cancer cells [27]; (c) intercellular and intracellular communication [28-32]; (d) cell adhesion [33]; and cell signaling [34].

In physiological conditions, membrane tethers can form both actively and passively. The active formation of membrane tethers is governed by (a) the polymerization of actin [28] or microtubules [29, 35] or by (b) molecular motors [35-37]. The passive formation occurs in course of leukocyte rolling, when they are pulled from preexisting membrane structures (i.e. microvilli) through specific receptor-ligand bonds upon contact with endothelial cells or platelets [26].

Tether formation requires changing the shape of the plasma membrane. Initiating a membrane tether from a flat region of the membrane requires modifying dramatically

its curvature. As the tether grows, phospholipid molecules flow from the flat region of the membrane into to tether, from a lower state of energy to a higher one. In case of artificial phospholipid vesicles, where parameters such as membrane composition and tension can be easier controlled, theoretical [38-41] and experimental work provided an accurate account of tether formation in terms of membrane tension and bending rigidity [37, 42, 43]. The situation with living cells is more complicated [43, 44]. The plasma membrane has a much more heterogeneous composition, with specialized domains (e.g. rafts) and a myriad of embedded molecular entities. It also interacts with the subjacent cytoskeleton. Unlike in artificial vesicles, in cells the membrane is not flat: could be highly convoluted, with intrusions and extrusions, and pre-populated with dynamic preexisting projections (i.e. cytonemes, microvilli, pseudopodes etc). As a consequence, tethers sprouting at distinct locations along the cell surface (e.g. apical and basolateral surface of epithelial cells [45, 46], microvilli [46], blebs [45], leading and trailing edge of migrating cells [33]) or from distinct intracellular membranes (e.g. Golgi versus endoplasmic reticulum [32]) could have differing material properties [34].

Membrane nanotubes have been extracted from vesicles or a wide range of cell types (red blood cells [47], neutrophils [48, 49], neurons [50], fibroblasts [51], as well as epithelial [45] and endothelial [52] cells) by special force transducers (optical tweezers [53-55], magnetic tweezers (vesicles only, [56]), aspirating micropipettes [48, 52, 57, 58]) and AFM [59]. With a few exceptions these studies have concentrated on single tethers pulled from particular locations [34]. Double tethers have been extracted from living cells [60, 61] and from synthetic vesicles by Cuvelier et al. [42].

Recent results suggest that multiple tether formation may be a control mechanism in physiological processes [25]. In particular, it was shown, that the number of tethers extracted from neutrophils in the course of their rolling increases with rising endothelial wall shear stress. The multiplicity (and thus the varying strength) of these transient attachments serves as a regulator of the cells' rolling under changing hydrodynamic conditions [24, 25]. Entire networks of membrane nanotubes have been observed in the interior of eukaryotic cells [30, 31] with likely role in the physical contact between intracellular membrane bound organelles. These findings suggest that cells can form and maintain multiple tethers and use them in various physiological processes.

Specific aims

The goal of this project was to get insight in the process of passive membrane tether formation. We were particularly interested to:

1. Determine the biophysical quantitative parameters associated with passive membrane tether formation: (a) tether elastic and (b) viscous coefficients, (c) relaxation time, (d) range of forces under which tethers can be pulled;
2. Investigate how these (above mentioned) parameters depend on the cell type;
3. Investigate the contribution of the actin cytoskeletal network in the membrane tether formation process.
4. Visualize the membrane tethers.

Experimental design

Cell culture and treatment

Two cell types have been used in this study: HB, a human brain tumor cell line provided by B. Hegedüs (National Institute of Neurosurgery in Budapest, Hungary, [62]), and Chinese Hamster Ovary (CHO) cells, purchased from the American Type Culture Collection (ATCC, Manassas, VA). Cells were grown at 37°C in 5% CO₂ on 75 cm² TC dishes in DMEM (Invitrogen Corp., Carlsbad, CA) containing 10% FBS (U.S. Bio-Technologies, Pottstown, PA), 10 µg/ml penicillin, streptomycin, gentamicin and kanamycin sulphate (Invitrogen Corp., Carlsbad, CA). Media were supplemented with 1 µg/ml Fungizone (Invitrogen Corp., Carlsbad, CA) for HB culture. 24 hours before an experiment, cells were plated on triangular glass coverslips (fabricated by cutting 18 mm square coverslips (Corning Inc., Corning, NY)), placed in 35-mm plastic Petri dishes and allowed to reach 30-50% confluence. Coverslips were then washed twice with PBS (Invitrogen Corp., Carlsbad, CA), transferred to CO₂ independent medium, containing 2% FBS and supplemented with antibiotics (as above). In cytoskeletal disruption experiments, HB cells were kept in CO₂ independent medium supplemented with LatA (Sigma, St. Louis, MO), a specific actin polymerization inhibitor (45–47) at 1.0 µM concentration for 30 min before the measurement.

Membrane pulling experiment

30 minutes before an experiment a suspension of 5-micron super-paramagnetic beads (concentration: 2×10^5 beads/ml in PBS; Dynabeads M-500, Dynal ASA, Oslo, Norway) was prepared. The bead solution was homogenized for 5 minutes with a Model 250 Brenson sonifier (Brenson, Danbury, CT). Immediately prior to an experiment, a

cell-plated triangular coverslip was transferred into the removable sample holder. The coverslip was covered with CO₂ independent medium then the sample holder mounted in its working position between the two poles of the MTW. About 10 μ l of the bead suspension was added on the coverslip. Beads, having density of 1.5 g/cm³, slowly descended on the coverslip and those that landed on cells, adhered to them. Beads typically were in contact with cells for 1 min prior to the application of the magnetic force. Experiments were conducted at room temperature. To identify a bead capable of pulling a tether, short magnetic force pulses (1 Hz, 50% duty cycle) were applied continuously while optically scanning the sample through the oculars of the microscope. To minimize the probability of rupturing the tethers during this search phase, the magnitude of these force pulses was small, typically 1-20 pN, corresponding to the minimum force which could visibly reversibly displace a bead attached to the membrane. Once a tether-pulling bead was identified, a long (typically 20 second) pulse, typically at a higher force was applied. Bead trajectories were acquired in bright field with a CoolSNAPfx digital video camera (Photometrics, Tucson, AZ), using a 20X objective.

Sample preparation for SEM

Cells were cultured (as described above) on 12-mm round coverslips instead of the triangular-shaped ones used in the other experiments. These were placed into a modified sample holder (to accommodate the round coverslips) beneath the plane of the magnetic poles of the MTW, thus creating a force on the magnetic beads oriented slightly upward (away from the coverslip). While applying a long continuous pulse, the sample was slowly raised above the plane of the poles. Unlike a triangular coverslip, a round coverslip does not fit well in between the poles. Therefore during the SEM experiments

beads were further from the poles and thus the magnetic force acting on them was smaller than in the regular tether pulling case described above. By this maneuver, the direction of the force was gradually changed from upward to downward (toward the coverslip). As a result, the beads eventually came in contact with the glass surface and adhered to it. Thus, the tethers extracted by the beads extended between two immobilized objects (the bead and the cell). Once this point was reached, the sample was fixed by adding 250 μ l of 2.5% glutaraldehyde (Electron Microscopy Sciences, Hatfield, PA) in PBS solution. Ten minutes after adding the fixative, the magnetic field was turned off and the coverslips transferred and kept in a Petri dish (containing the same fixative) for an additional 80 minutes. The fixative was then removed by 3 rinses in PBS, the coverslips transferred into a holder and plunged for 30 minutes in an increasing concentration series of ethanol as follows: 10%, 25%, 50%, 75%, 95%. Finally, the holder was kept in 100% ethanol overnight. The dehydration of the sample was completed in a Samdri-PVT-3B (Tousimis, Rockville, MD) critical point drier by exchanging ethanol to liquid CO₂ and sublimating the latter. The coverslips were attached to stubs using carbon adhesive tabs; the surface of each coverslip was connected at the edge through 3 copper strips to the stub, to provide maximal electrical conductivity. The samples were sputter coated with platinum at 5 mA for 45 seconds before examination with a Hitachi S4700 cold-cathode field-emission scanning electron microscope at an accelerating voltage of 5 kV.

Data analysis

Time-displacement trajectories of the beads were fit during the creep ($F \neq 0$) with the simplest phenomenological model, which provided the elastic and friction

coefficients of the tethers, along with the relaxation time and their number at the beginning of the pulling.

Results

Tether manifestation in magnetic tweezers experiments

Membrane tether extraction took place under constant force applied to the magnetic bead (see Fig. 13 for schematic representation of the process) whose position was recorded as function of time (see Fig. 14 for typical bead trajectories). On each coverslip, several beads have been identified as tether-pulling during the searching phase. The probability of finding tether-pulling beads was higher in case of HB cells (quantification not shown). All the tether-pulling beads had a low amplitude ($\sim 0.1 \mu\text{m}$) thermal movement in between pulses, when no force was applied (similar to the finding reported in [55]). Upon applying the magnetic force, the bead starts moving along its direction with no lag, initially faster then slower. Once the magnetic force is stopped, the bead retracts towards its original location. Some beads went out of the field of view during creep and never returned (tethers broke). During the creep, the trajectory often revealed multiple sudden jumps in the bead velocity. Some trajectories were smooth, with no jumps. The jumps were associated with the rupture of individual tethers (under the assumption that multiple tethers were pulled at a time). On the basis of the ruptures, numerous (in the range of tens) and long (in the range of 100 microns) tethers were identified. Scanning electron microscopy observations (Fig. 16) confirmed the connection between the bead and the cell through multiple nanotubes originating from the cell membrane.

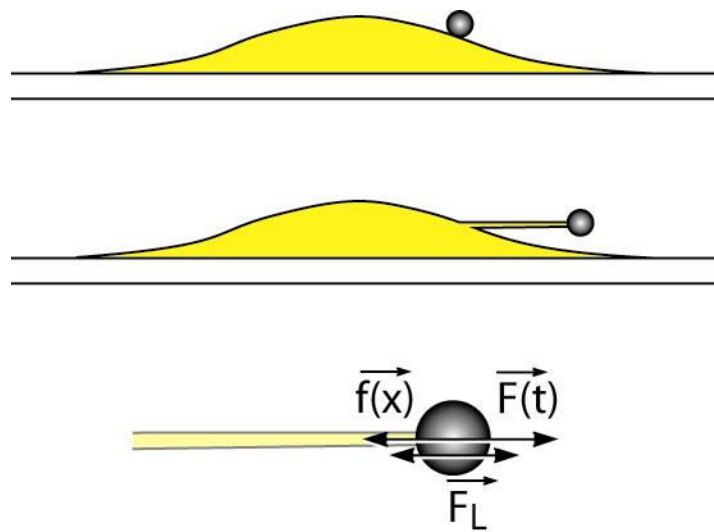


Figure 13. Schematic illustration of extracting a membrane tether by magnetic tweezers. $F(t)$ represents the magnetic force (which is a function of time), $f(x)$ the tether force (the force exerted on the bead by the membrane tether, a function of tether length), and F_L a random thermal fluctuating (Langevin) force (neglected in the membrane tether formation study but essential for the Crooks fluctuation theorem verification, see next section).

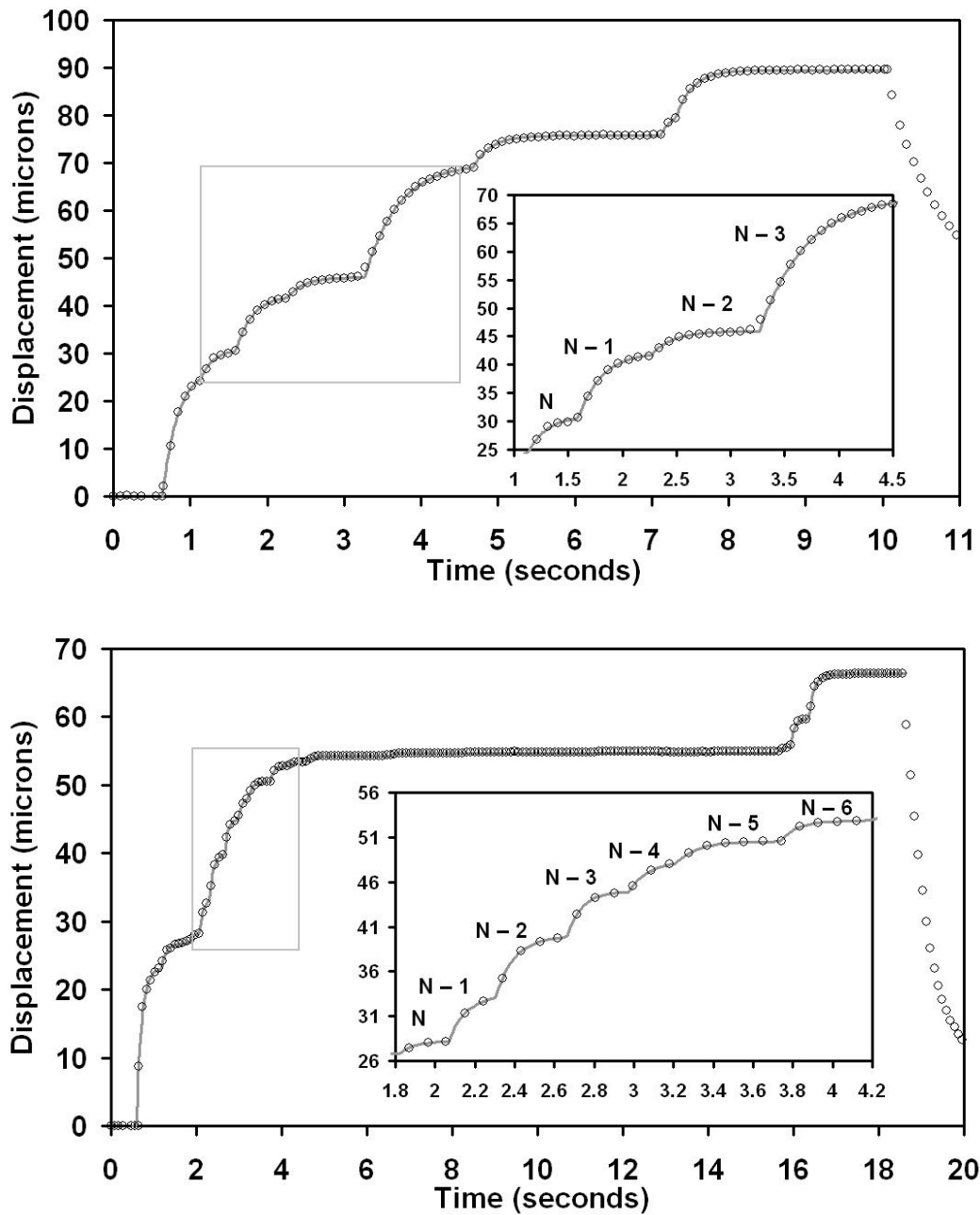


Figure 14. Typical time-displacement curves in membrane tether pulling experiments.

“0” on the vertical axis corresponds to the position of the bead before the application of the force pulse. The open circles represent data, the lines over data points are the result of modeling (discussed later in the text, where the meaning of the labels N , $N-1$, etc., is also given). *Upper panel.* HB cell. *Lower panel.* CHO cell

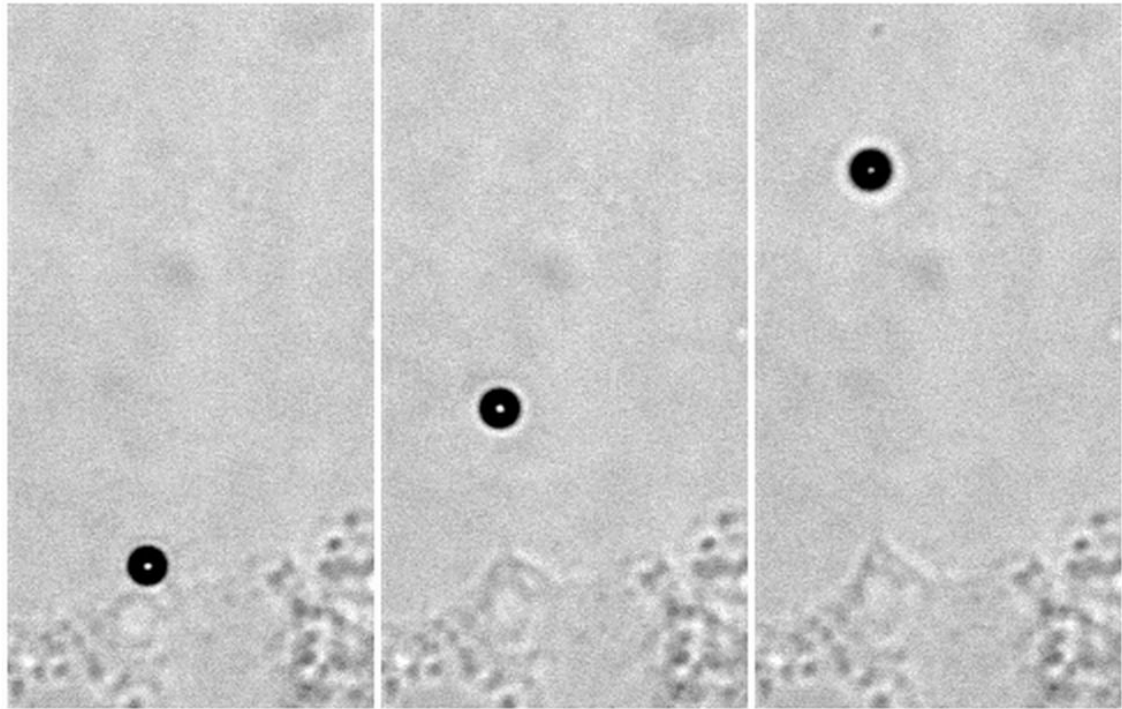


Figure 15. Membrane tethers: optical microscopy.

Video sequence before (left panel) and during (middle and right panels) applying a force pulse (HB cells, bright field microscopy, 20x objective). Scale is given by the 5-micron bead.

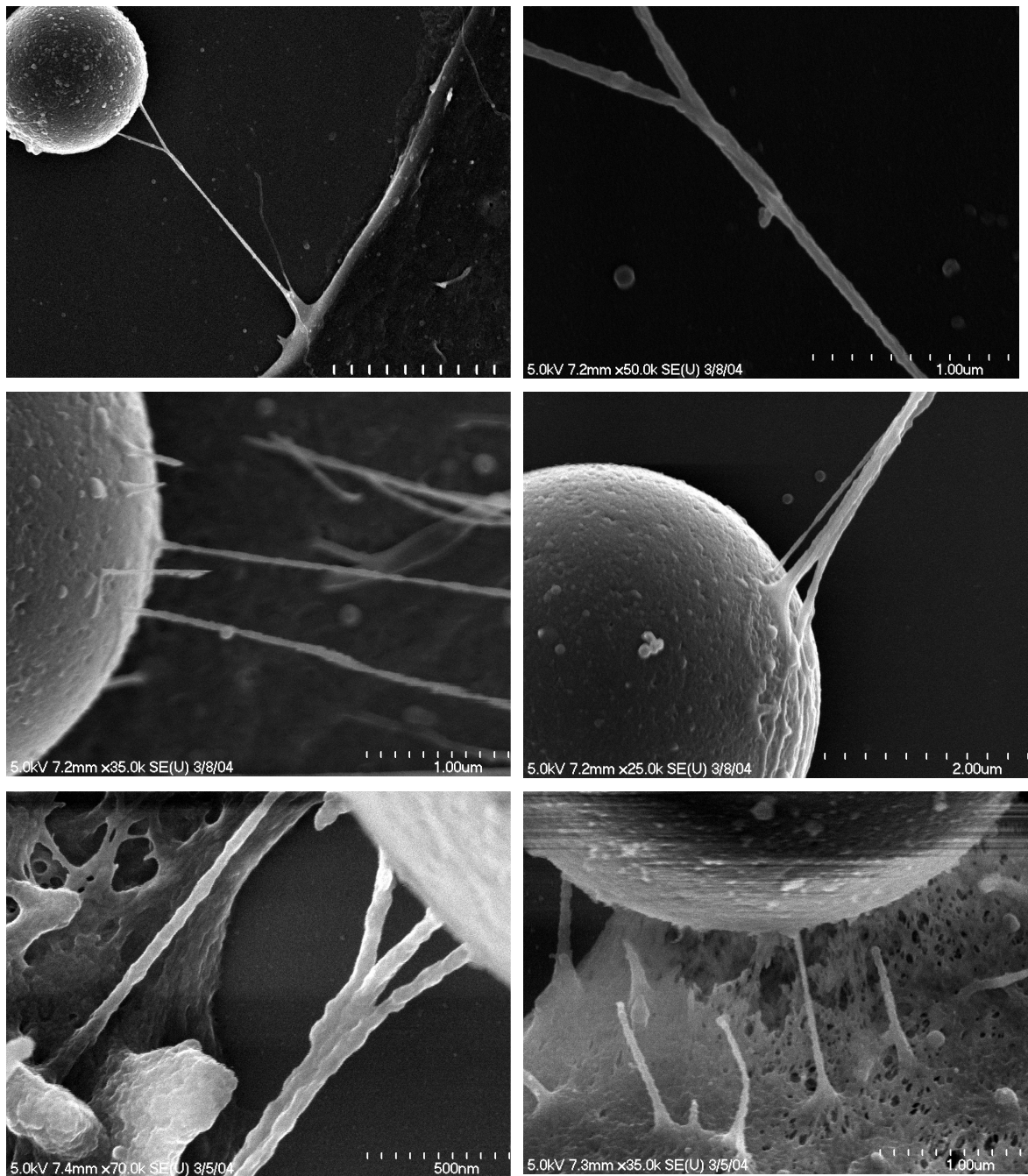


Figure 16. Membrane tethers: field emission scanning electron microscopy (FESEM).

Upper panel. Left: two tethers connecting the bead to a HB cell, one of them broken. Right: detail of the merging point. *Middle panel.* Left: About 6 tethers connected to the bead (some of them broken; HB cell). Right: Multiple tethers connected to the bead (HB cell). *Lower panel.* Left: bundle of three tethers connected to the bead (HB cell). Right: multiple tubular structures connecting the bead to the cell (CHO cell).

Comparison of figures 14 and 16 strongly suggests that the jumps correspond to the detachment or rupture of individual tethers. Similar discrete events have been observed in the velocity of leukocytes rolling on selectin coated surfaces and also interpreted in terms of multiple bonding between the cell and the substrate [24]. Since the magnetic force exerted on the bead is constant along its entire trajectory, when one of the tethers ruptures, each remaining tether experiences a larger force (the same force is distributed to fewer tethers). Thus, the bead accelerates and moves with a larger velocity.

Modeling tether formation

Deformable cells are viscoelastic materials. Thus the motion of a tether-pulling bead is typically analyzed in terms of viscoelastic circuits built of springs and dashpots, as representations of elastic and viscous properties, respectively [63].

Segments between two subsequent abrupt changes in slope along bead trajectories, $x(t)$ in Fig. 14, were approximated with simple exponentials (lines over data points):

$$x(t) = A \left(1 - e^{-(t-t_0)/\tau} \right) \quad (5)$$

The quantity t_0 denotes the time where the exponential function used for the fit of a given segment would cross the horizontal axis. In case of the first segment, t_0 is the moment the magnetic force was applied, as determined by the magnetic tweezers control application (see “Magnetic pulse/camera exposure timing”, above); in the rest of segments, it is a fitting parameter. To relate the fitting parameters to physical quantities, we used a minimal model of multiple tether formation (Fig. 17): in which each of the N

initial tethers is represented with an identical Voigt body (a dashpot, characterized by a friction constant μ , in parallel with a spring, with spring constant k), a widely used element in phenomenological models of viscoelasticity [63]. The friction between the magnetic bead and the cell culture medium is represented by μ_m ($\mu_m = 6\pi\eta R$, $R = 2.5$ micron is the radius of the magnetic bead, and $\eta \approx 10^{-3}$ Pa s is the viscosity of the culture medium, approximately that of water). This simplification is equivalent to assuming that the different tethers are identical (are composed of the same material) and do not interact. Solution of this model provides the same exponential form as above and identifies the constants in that expression in terms of the model parameters:

$$A_i = F / [k(N - i)] \quad (6)$$

and

$$\tau_i = [\mu + \mu_m / (N - i)] / k \quad (7)$$

where A_i and τ_i correspond to the bead trajectory after $i(= 0, 1, \dots, N - 1)$ tethers have ruptured, and F is the constant force exerted by the magnetic tweezers on the magnetic bead.

To estimate the total number of tethers, N , pulled in each experiment we considered A_i as a continuous function of its index and fit the experimental results for this quantity to the hyperbola, as given by the model. The outcome of this procedure, shown in Fig. 18, provides values for k , N and μ (for the latter through the experimentally determined $\tau_i = [\mu + \mu_m / (N - i)] / k$) listed in Table 1. For the above analysis of N only curves with at least three ruptures were used.

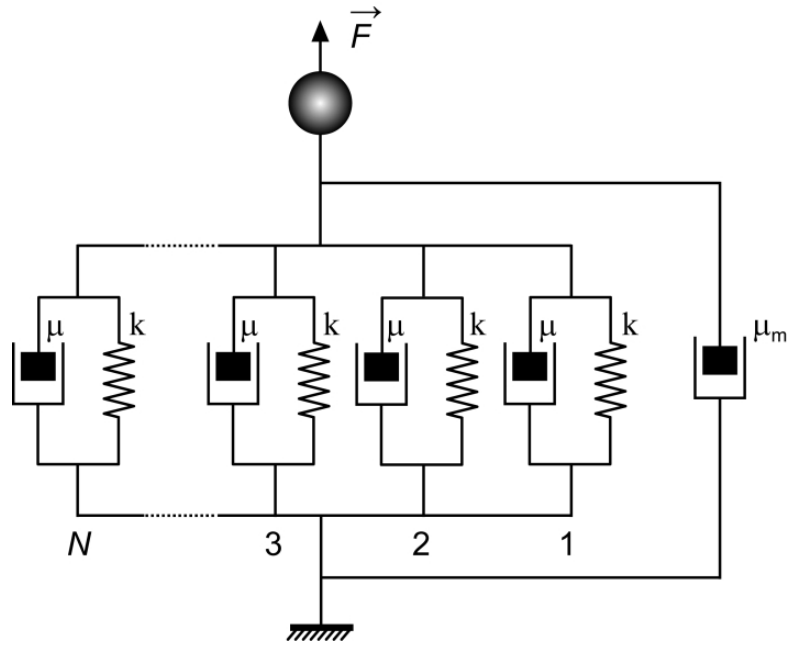


Figure 17. Voigt model for multiple tether formation.

Each Voigt body (a dashpot with friction constant μ and spring with spring constant k) represents one of the N tethers. Tethers are assumed to be identical, non-interacting and detach one by one during the pulling experiment under the constant force F . μ_m represents the friction coefficient between the magnetic bead and the culture medium .

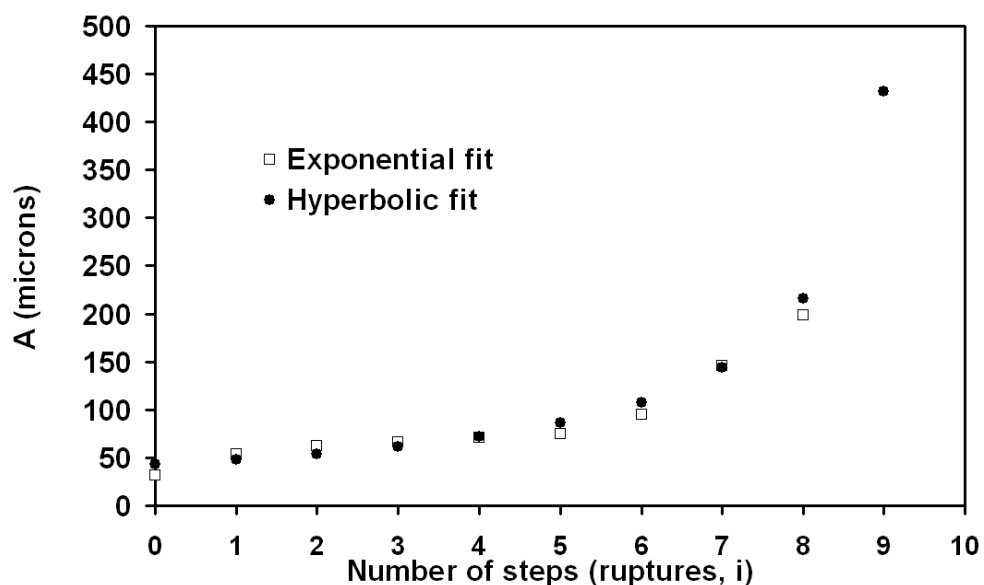
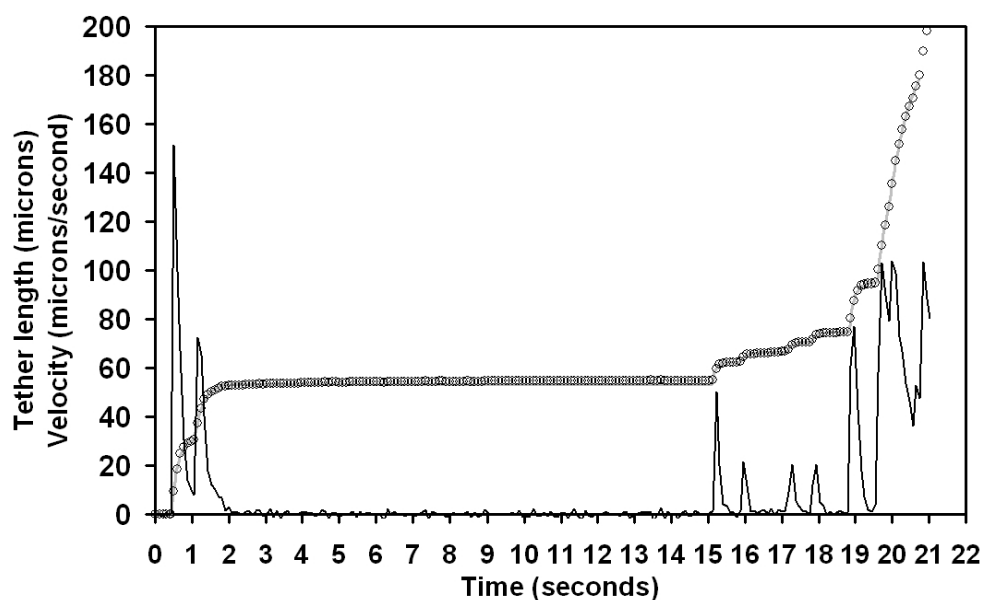


Figure 18. Estimating the total number of tethers.

Upper panel. Typical bead trajectory (open circles) fit with the Voigt model for multiple tether formation (line over data points). The spiky curve represents the bead's instantaneous velocity. *Lower panel.* The parameters A_i ($i = 0, 1, \dots, N-1$) obtained from the exponential fit to data (open squares) and deduced from the hyperbolic function $A(x) = F/[k(N-x)]$ as result of modeling (filled circles; see text). The hyperbolic fit provides the total number of tethers, N ($= 10$ for the shown curve) at the beginning of pulling and the ratio F/k , and thus k .

Effect of cytoskeleton disruption

Actin cytoskeleton involvement in the process of membrane tether formation has been investigated by repeating the experiments on LatA treated HB cells. Actin cytoskeleton disruption with LatA did not affect either μ or the force per tether, but resulted in the increase in k (see Table 1 for all quantitative results).

Table 1. Summary of the quantitative results obtained in membrane tether study

Cell type (treatment)	μ	k	N	τ	F	A
	(pNs/ μ m)	(pN/ μ m)	(Mean \pm SEM)	(sec)	(pN)	(μ m)
	(Mean \pm SEM)	(Mean \pm SEM)	(Mean \pm SEM)	(Mean \pm SEM)	(Mean \pm SEM)	(Mean \pm SEM)
HB (control) n = 113 tethers, 16 cells	(1.2 \pm 0.5) $\times 10^{-2}$	(4.5 \pm 1.0) $\times 10^{-2}$	16 \pm 2	0.28 \pm 0.05	2.1 \pm 0.3	59.2 \pm 3.5
HB (LatA) n = 106 tethers, 16 cells	(1.1 \pm 0.2) $\times 10^{-2}$	(8.4 \pm 1.3) $\times 10^{-2}$ *	14 \pm 2	0.12 \pm 0.02*	2.9 \pm 0.4	30.5 \pm 8.3*
CHO n = 85 tethers, 7 cells	(7.9 \pm 1.3) $\times 10^{-2}$ *	(4.9 \pm 0.3) $\times 10^{-1}$ *	26 \pm 5*	0.15 \pm 0.02*	7.7 \pm 1.9*	16.3 \pm 4.2*

* = significantly different from HB control ($p < 0.01$)

N = the number of tethers at the beginning of the pulling

F = average force/tether at the beginning of the pulling

A = terminal tether length before the first rupture (fitting parameter)

Discussion

The magnetic tweezers experiments, in combination with optical microscopy and SEM allowed the direct visual observation of multiple tethers (Figs. 15 and 16).

A simple model of viscoelasticity (Fig 17) allowed determining the total number, N , of tethers in individual pulling experiments (Fig. 18). The values of N , obtained from the model varied between 12-48 and 9-34, respectively for the CHO and HB cells. The largest number of experimentally clearly discernable rupture events was 22 for CHO and 12 for HB cells. The number of MTW tethers in each individual experiment is consistent with the relatively large diameter of the magnetic bead (5 μm), which can easily accommodate binding sites for several tethers. The plateau values of the bead displacements seen in Fig. 14 prior to ruptures correspond to the maximum length of the “tether-springs” under the applied force. As more tethers rupture and the force per tether increases, so does the terminal length of the remaining ones (i.e. A_i increases with i).

Tether formation requires initiation. The contact between the force transducer and the membrane material was established by the gravitational fall of a magnetic bead (5 μm diameter, 1.5 g/cm^3 density) through tissue culture medium, producing an overall force on the cell of < 1 pN. Producing tethers does not require any detectable initiation force no matter how many are produced. This is an indication that they originate from pre-existing structures (in which the plasma membrane is already highly curved), possibly microvilli, which the magnetic bead contacts during its gravitational descent (and with which it establishes practically force-free contact).

It has been postulated that tether formation is associated with three sources of friction (viscous resistance): (1) a viscous drag between the inner monolayer of the bilayer membrane and the cytoskeleton, (2) a viscous slip between the two monolayers of the membrane and (3) the surface viscosity of the membrane [47, 64]. According to the

current view, there are no cytoskeletal filaments inside passively formed tethers [47, 65]. However, the probability of forming a tether with a constant force increased dramatically with drugs that disrupt the actin cytoskeleton, like cytochalasin B or D, LatA and dimethylsulfoxide (DMSO) [53]. Since membrane tethers could originate from microvilli [24] cytoskeletal filaments or their residues could be present inside the membrane tube. Cytoskeletal filaments, if indeed present, might represent an additional source of friction. In our experiments, LatA treatment did not significantly change the friction constant, showing that the cytoskeleton involvement in the process of tether formation is not relevant. Similar results were reported in [55]. Authors of that work used optical tweezers to extract single tethers from terminally differentiated fibroblasts and mesenchymal stem cells (MSC). The probing beads (of smaller dimension, 0.5 μm) were attached to cells by gravitational fall, like in magnetic tweezers experiments. It was found that single membrane tethers could be extracted with very low forces (~ 3 pN), without any initiation force. Cytoskeleton disruption had no effect on MSCs. In particular the tether force and tether length did not change, whereas these quantities decreased in case of fibroblasts. Even though the tether friction coefficient was unaffected by LatA treatment in case of magnetic tweezers experiments, the resulting tethers had shorter length under the same force (as assessed by their equilibrium length before the first rupture; Table 1) and were stiffer (k increased; Table 1). This suggests that LatA treatment results in the decrease in the MTW membrane reservoir. A possible reason for this is the known property of this drug to modulate the cell's osmotic homeostasis by activating the Na^+ channels in the plasma membrane [66, 67], which induces osmotic cell swelling thus decreasing the membrane reservoir. It is worth noting that stem and tumor cells do have common

properties: neither cell type has the features of terminally differentiated cells. Tumor cells start out as differentiated cells but, due to their rapid proliferation, gradually lose their original lineage specification.

Crooks fluctuation theorem verification at cellular level

Background and significance

Fluctuation theorems relate the free energy difference between two equilibrium states of a system to a certain average of the work along non-equilibrium paths which connect the two states. They have been successfully applied to interpret single molecule pulling experiments. For instance, the folding free energy of a RNA hairpin has been determined from repeated folding/unfolding force-extension measurements [23] by employing the Crooks fluctuation theorem [68]. This theorem, applicable in microscopic systems driven reversibly between two equilibrium states by an external perturbation through non-equilibrium intermediary states, predicts that:

$$\frac{P_F(W)}{P_R(-W)} = e^{W_D} = e^{(W-\Delta G)} \quad (8)$$

where $P_F(W)$ is the probability distribution of the values of the work during the forward (F) processes, $P_R(W)$ is the probability distribution of the values of the work during the reverse (R) processes (determined as the result of an infinite number of experiments), W is the dissipative work and ΔG the free energy difference between the final and the initial states.

In order for the theorem to apply, the process has to be reversible. That is, if the system evolves from an initial equilibrium state (A) to a final equilibrium state (B) as a result of varying a control parameter, then changing the direction of variation of the control parameter results in driving the system backwards, from the final equilibrium state (B) towards the initial one (A). Whether the two equilibrium states (A and B) have to be the same in each F-R cycle, the intermediate states of the system driven from A to B and vice-versa do not. Moreover, the system does not have to reach the equilibrium as soon as the controlling parameter reaches its final value (it actually cannot, since the control parameter is varied at a rate higher than the capacity of the system to adapt, it follows a non-equilibrium path). After the control parameter reaches its final value, the system continues to relax until it reaches its equilibrium state. For the purpose of calculating ΔG by using the Crooks fluctuation theorem, this relaxation phase is not relevant, as it does not have any contribution to the work between the two states. However, it is essential that (1) the system always start from equilibrium, (2) reach (eventually) a final equilibrium state and (3) the control parameter go through the same intermediate values in both F and R processes.

In the case of the RNA hairpin mentioned above [23], a large number (at the order of 10^2) of folding/unfolding experiments were carried out. The molecule, stretched between two latex beads, was pulled (unfolded) with constant velocity with an optical tweezers, while monitoring the force exerted on the bead by the molecule. In the R process, the molecule was let fold back, by changing the direction of the control parameter (velocity). The two work distributions $P_F(W)$ and $P_R(-W)$ depended strongly on the pulling protocol (i.e., the pulling speed). According to equation (8), when the two

work distributions $P_F(W)$ and $P_R(-W)$ are equal, $W = \Delta G$. Thus, ΔG can be determined by simply finding the point where the two work distributions cross. Despite $P_F(W)$ and $P_R(-W)$ being strongly dependent on the pulling speed, the crossing point between the two (i.e., ΔG) was the same for each pulling velocity. Thus, the free energy difference did not depend on the pulling protocol, proving that the Crooks fluctuation theorem is valid in the single molecule pulling.

To determine ΔG through this method, a relatively large number of pulling experiments is necessary. The two distributions cross towards their tails, where fewer events occur. Therefore, one needs a large number of experiments to make sure the tails are correctly represented.

In case of membrane tether pulling, carrying out a large number of experiments is a challenging issue, because tethers have the tendency to break, thus the system changes. To be able to apply the Crooks fluctuation theorem in case of membrane tethers (a much complex structure than a single molecule), we have to resort to a method in which a smaller number of pullings is sufficient.

Kosztin et al. [69] noticed that, under the assumption of “stiff spring approximation” (which states that the force transducer is connected to the biological sample through a “spring” with infinite spring constant), the probability distributions of work is approximately Gaussian. Statistically, these samplings will fall around the average values of the work (see Fig. 19), allowing a rapid estimation of the average. The change of free energy in this case is:

$$\Delta F = (\overline{W}_F - \overline{W}_R) / 2 \quad (9)$$

(see [69] for details).

Stimulated by the recent demonstration of Crooks fluctuation theorem at single molecule level summarized above [23], we designed experiments to investigate the validity of the theorem single cell level, in the process of membrane tether formation (a joint project with Dr. Ioan Kosztin).

Specific aims

The overall goal of this project was to test the validity of Crooks fluctuation theorem at cellular level, by employing the membrane tether formation process and the FR method. Particularly:

1. Check if the change of free energy ΔG , as calculated through the FR method, is independent of the pulling protocol (switching time between the two equilibrium states) and, if so,

2. Reconstitute the free energy profiles (ΔG vs. tether length) of the membrane tethers by tether pullings between multiple pairs of equilibrium states.

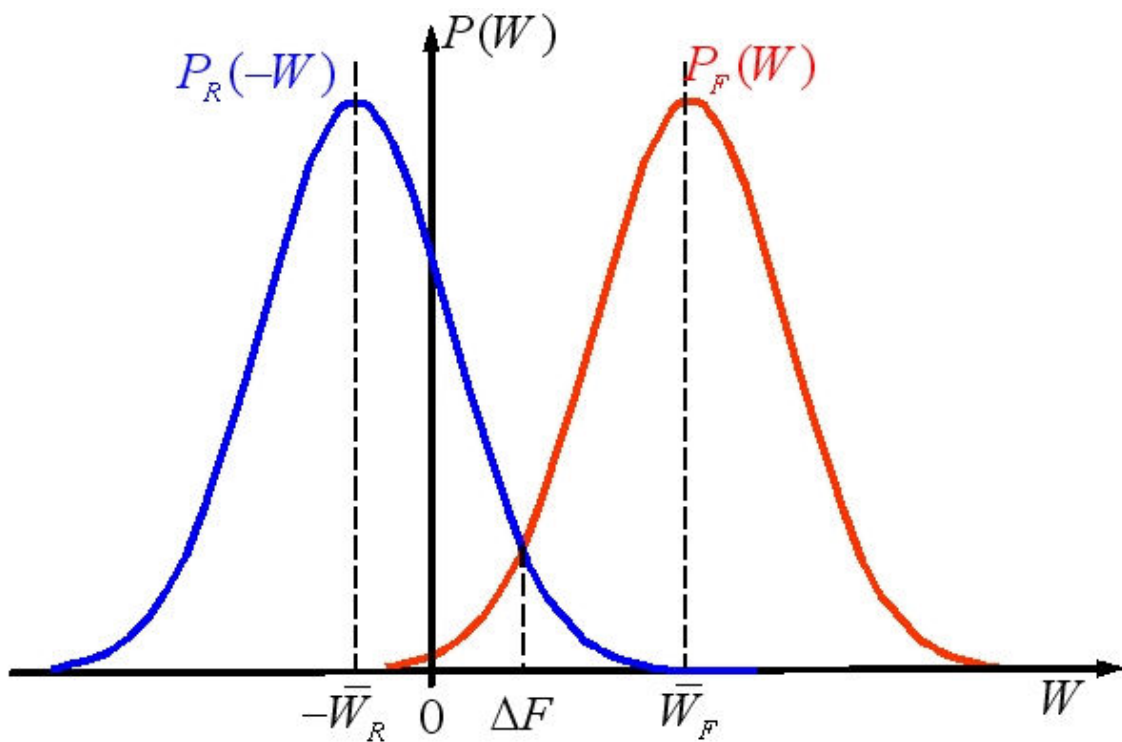


Figure 19. FR method to calculate the potential of mean forces.

A relatively small number of samplings (which would probably fall around the peak value of each distribution) is sufficient to determine the point where the two distributions cross, under the assumption that the F and R work distributions are identical shifted Gaussians (Kosztin et al., 2006 [69]).

Experimental design

In our setup, the tether pulling experiments take place under constant force (as opposed to the RNA folding/unfolding experiments described in [23], which are carried out under constant velocity). Therefore, in the case of magnetic tweezers, the control parameter (i.e., the independent variable) is the force, not the displacement. In turn, the measured parameter (i.e., the dependent variable) is the tether length (bead displacement). The two equilibrium states of the tether system correspond to its equilibrium length at two given stretching forces (as shown above, tether length equilibrates at a given applied force). “Tether system” here refers to a bundle of tethers stretched between a cell and a magnetic bead; the number of tethers within a bundle cannot be controlled.

To initiate the tether formation, a small step force is applied to the bead (corresponding to a current of 0.2 A). Once the tether system equilibrates at a certain length, the forward (F) then the time-reversed (R) non-equilibrium transitions are generated by varying at constant rate the current between the initial value of 0.2 A and a final value corresponding to a higher value of the force. Note that the actual experiment control parameter is the current, not the force. Even though a higher current always corresponds to a higher value of the force at a given location, the two are not necessarily proportional. This does not have any negative impact on the result as long as the R process is the time reverse of the F process. Once the higher force value is reached, the system is let equilibrate (as mentioned in [23] and above, the system does not have to reach the equilibrium at the same time as the control parameter). A typical force (current)

profile and a trajectory recorded during a preliminary experiment are shown in the upper panel of Fig. 20. The tether length (bead trajectory) for each FR cycle is plotted with respect to the applied force in the lower panel. One FR cycle represents a full F process ($dt1F + dt2F$) followed by a full R process ($dt1R + dt2R$, see the time denominations in the upper panel of Fig. 5). For each individual FR cycle in Fig. 20 (lower panel), the work is calculated according to the formula:

$$W = \sum_{i=1}^N F_i (x_i - x_{i-1}) \quad (10)$$

where F_i is the value of the force, x_i and x_{i-1} are the length of the tether in two consecutive frames and N is the total number of data points (i.e. camera frames – of the order of thousands per experiment). Note that there are 22 superimposed curves in Fig 20, 11 corresponding to the F (dotted lines) and 11 to the R (solid lines) processes.

To prevent the tethers from rupturing, the equilibrium forces are kept at low values, by choosing cells located as far as possible from the poles along the y axis.

In the experiments designed to determine ΔG for two switching times ($dt1F,R$) between the two equilibrium forces, the two corresponding FR cycles were applied alternatively: one FR cycle for 1 s, followed by one FR cycle for 4 s. This minimized the bias between the two switching time experiments related to the tether system getting older (tethers have the tendency to get “looser” after repeated pullings). The two cycles (1 and 4 s) were repeated 11 times (see Fig. 21). In the experiments designed to reconstitute the free energy profiles, the upper equilibrium force was increased gradually from cycle to cycle; the rate of varying the force was constant. Successions of 6 FR cycles (each

cycle corresponding to a higher upper equilibrium force) were repeated 11 times (see below).

All experiments were performed on HB cells, in the same conditions as in the previous section (if not specified differently). Data processing was carried out in Labview.

Results

Free energy dependency on the switching time

As hypothesized, results showed that the Crooks fluctuation theorem is valid at cellular scale. More precisely:

1. The hysteresis between the F and R processes increased with the decrease of the switching time (i.e., with the degree of departure from equilibrium, see Fig. 22);
2. The calculated free energy difference is switching time-independent (Fig 23).

Free energy profile reconstruction

To determine the free energy profiles of the tethers as a function of tether length, the higher equilibrium force was varied along an experiment, as exemplified in Fig. 24. The free energy profile determined through 14 different experiments is depicted in Fig. 25. Even though, in principle, the individual tethers can be approximated as identical, the 14 curves depicted in Fig. 25 (on a log-log scale) look quite different, for two reasons:

1. The magnetic force applied to the bead was different in different experiments;
2. The number of tethers pulled in each experiment was also different (therefore, individual tethers experienced different values of force/tether, hence different length under the same total force).

The log-log representation of the experimental data in Fig. 25 (each experiment composed by 6 data points, corresponding to 6 force intervals) could be fit very well with lines:

$$\Delta G = ax + b \quad (11)$$

where a and b are linear fitting parameters.

The mean value of the slope (fitting parameter a) in all linear fits was ~ 2 (1.94 ± 0.14 , average \pm SD).

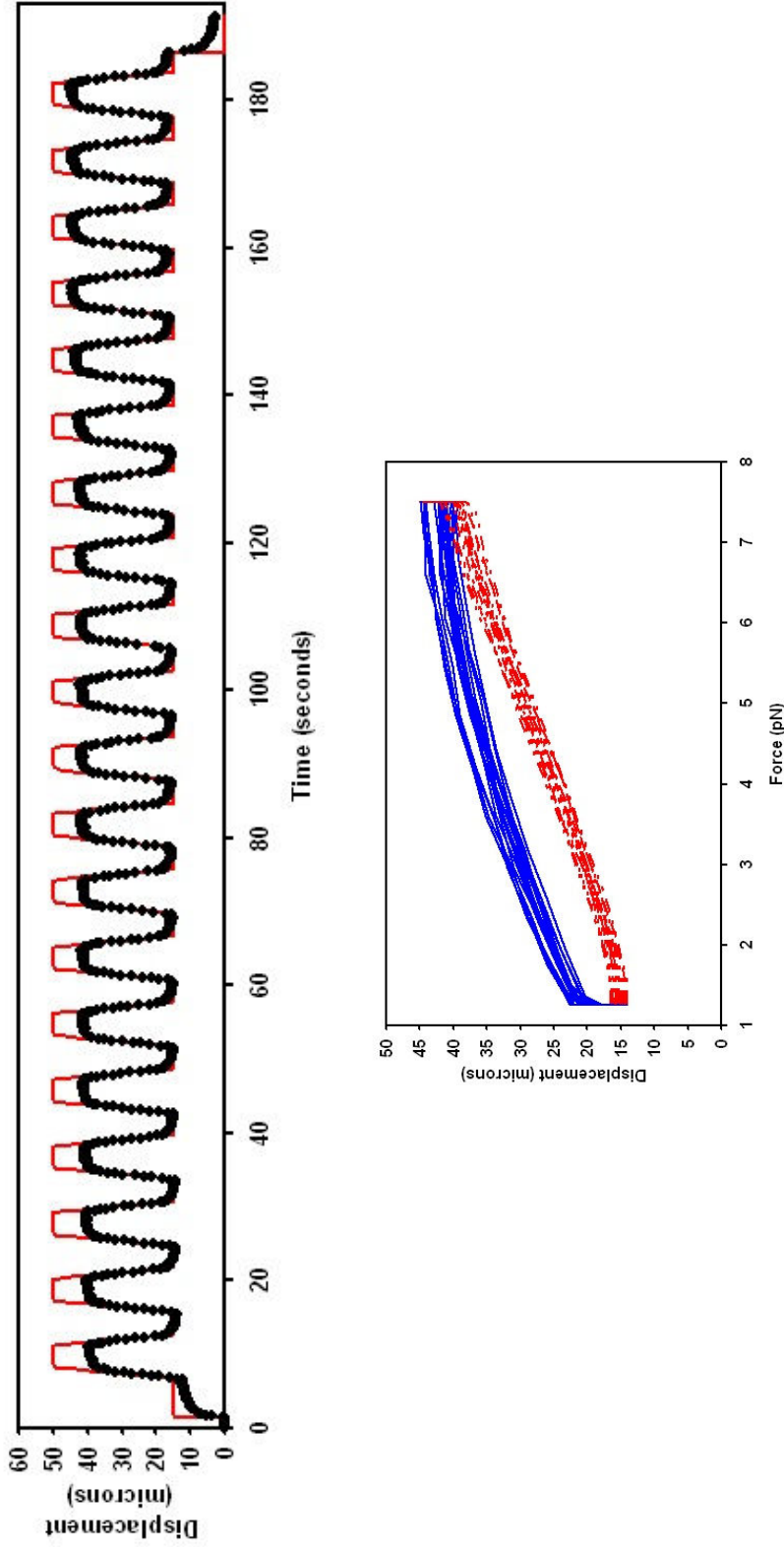


Figure 20. Experimental design for Crooks fluctuation theorem verification.

Upper panel. The magnetic force, controlled by the current through the coils (solid red line) is varied between a lower and a higher value according to a given protocol (typically a ramp characterized by a switching time – dtIF,R in Figs. 4 and 5). Black filled circles are the bead trajectory. *Lower panel.* Plot of bead displacement (tether length) vs. applied force for each FR cycle in the curve in upper panel. Blue solid lines represent the bead trajectory during the ascending and upper plateau segments of the force profile (F). Red interrupted line represents the descending and lower plateau segments (R). (20 FR cycles superimposed; note that in each cycle the bead moves slightly differently - the bead trajectories do not perfectly superimpose).

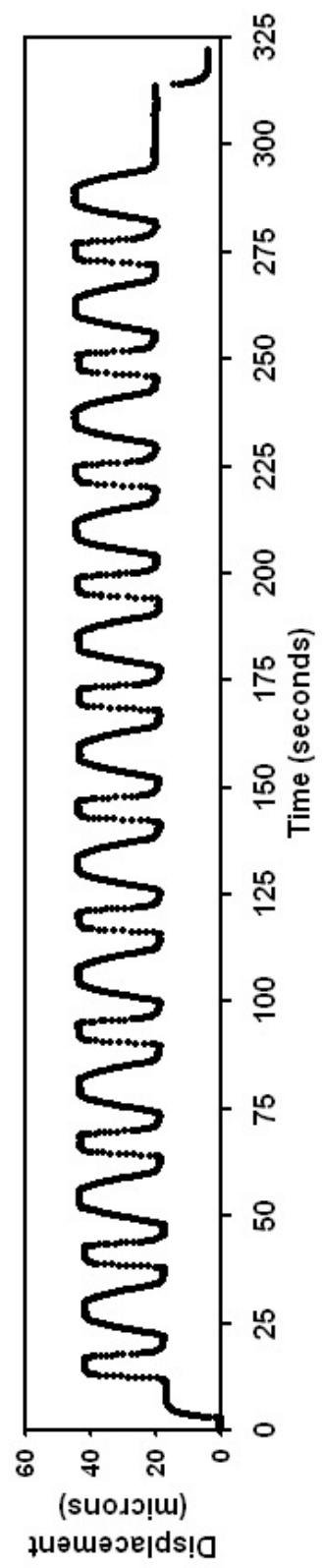
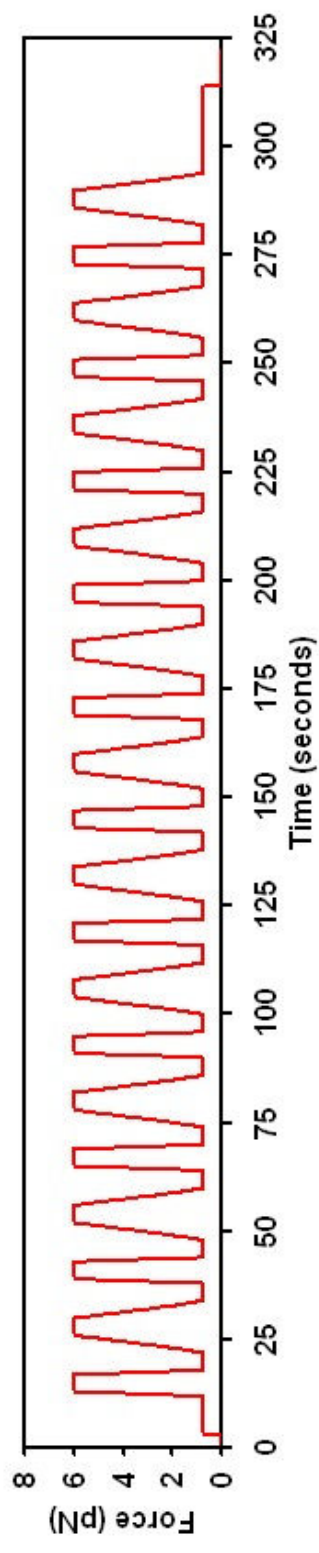


Figure 21. Force profile and typical displacement curve for two switching (1 and 4 s) times between two given force values. 22 FR cycles (11 for each switching time) are applied to the tether system.

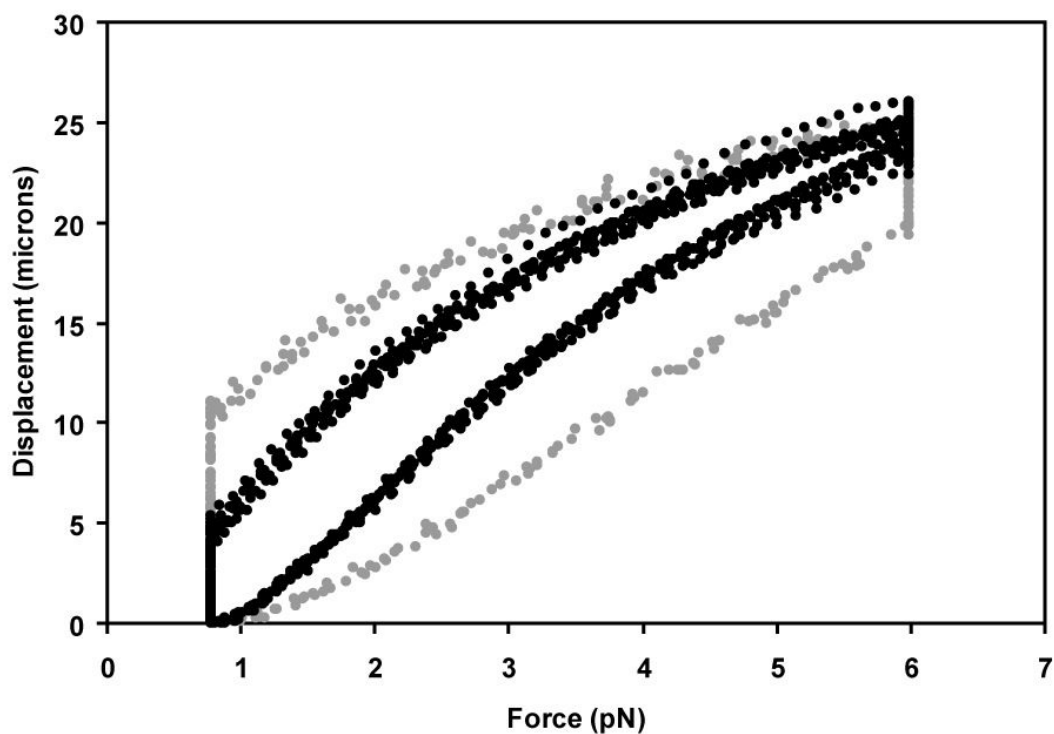


Figure 22. Force-displacement curves for the experiment depicted in Fig. 21.

Black filled circles: 4 s switching time data set. Grey filled circles: 1 s switching time data set. Each data set is composed of 11 superimposed FR cycles. Within each data set, the lower and the upper edges of the cycle represent the F and R process, respectively. The two vertical edges correspond to the constant force regimes, where tether length equilibrates after the force reached the final value (right and left edges, respectively). Note that the degree of departure from equilibrium (the hysteresis, i.e. the area circled by the data) is larger for the lower switching time.

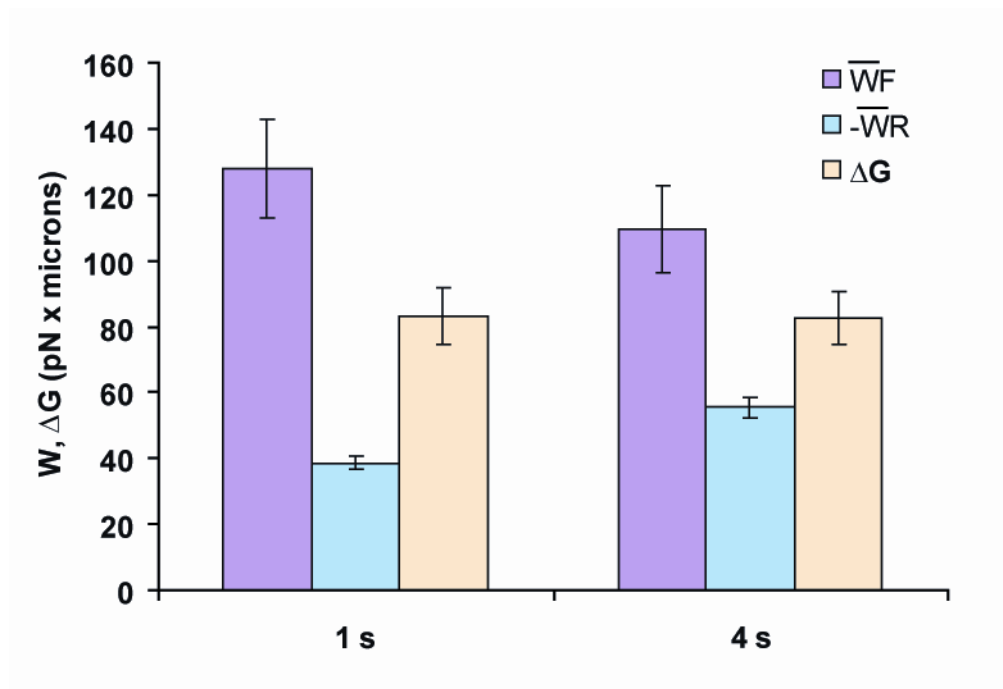


Figure 23. The variation of free energy associated with the tether pulling process, as determined through the FR method.

Note that the change of free energy ($\Delta G = (\overline{W}_F - \overline{W}_R)/2$) does not depend on the switching time. For each switching time, the columns are (from left to right): \overline{W}_F , \overline{W}_R and ΔG .

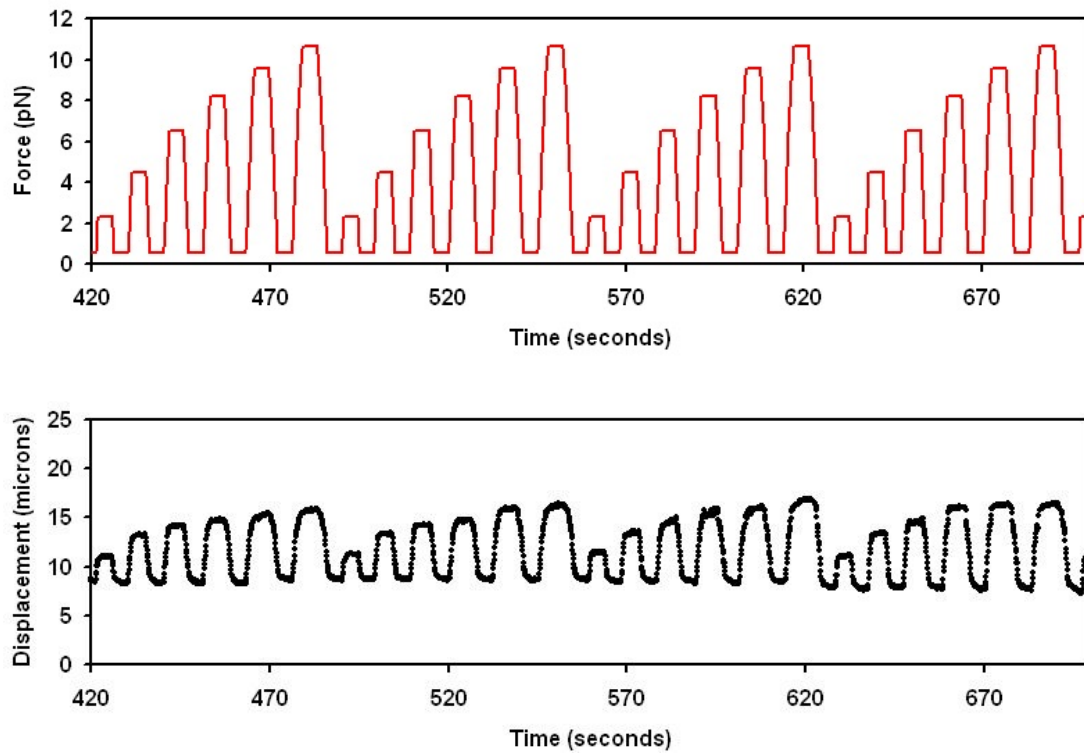


Figure 24. Force profile and typical bead displacement for reconstruction of free energy profiles.

Upper panel. Force profile: successions of 6 FR cycles between a lower and 6 different force values are applied to the sample. The force ramp is constant in each cycle. *Lower panel.* Bead trajectory under the force profile in the upper panel.

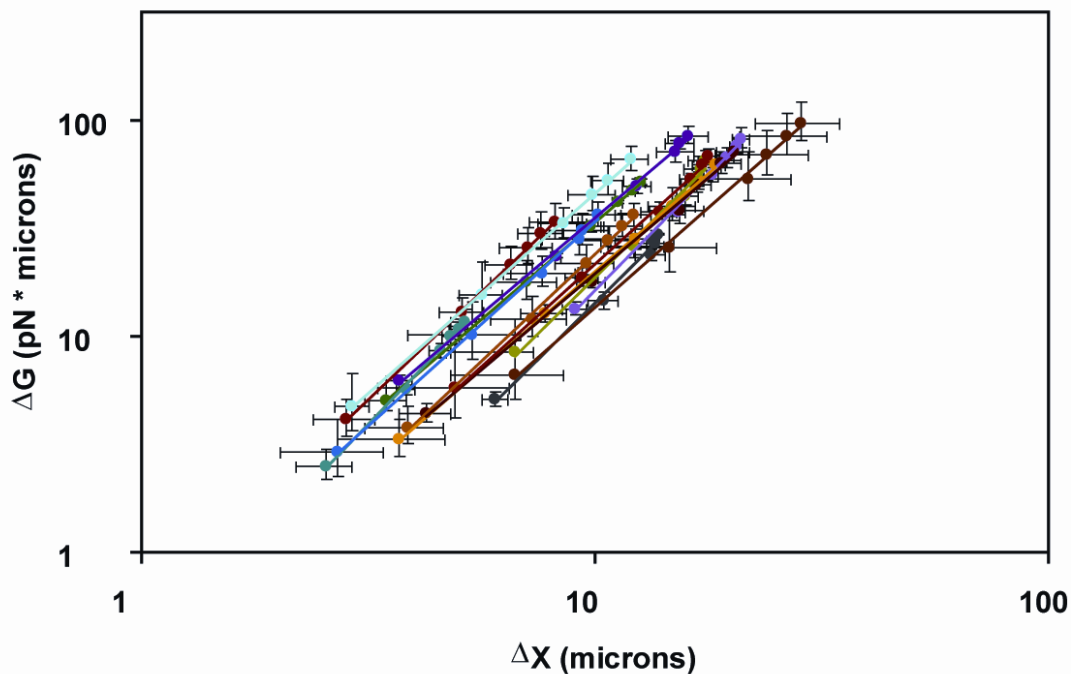


Figure 25. Free energy profile vs. tether length (n = 14 experiments).

Data points along one fit line are one experiment. There are 6 data points/experiment, each data point corresponding to one of the 6 force intervals. One data point represents the average ΔG for the number of corresponding FR cycles within an experiment. The solid lines are linear fits. Error bars are SD.

In an attempt to check the consistency of these results with the ones obtained in the previous study (in which individual membrane tethers were considered as Voigt bodies with given friction and spring constants), we tested the same mechanical analogy.

The curves in Fig. 25 are determined by points representing the system in equilibrium states (corresponding to tethers of fixed length), therefore only the elastic behavior is obvious. Since the slope coefficient (fitting parameter a in eq. (11)) is ~ 2 , the lines in Fig. 25 can be considered as potential elastic energy of extended tether-springs:

$$\Delta G = N \left(\frac{1}{2} k \Delta x^2 \right) = \frac{1}{2} (Nk) \Delta x^2 \quad (12)$$

where N is the number of tethers in a bundle, k is the spring constant of one membrane tether in the bundle, and Δx the tether length change.

Equations (11) and (12) allow estimating the product Nk . The average value of Nk for the curves in Fig 25 is 1.09, a number of the same order of magnitude with the one calculated from Table 1 (0.72).

Conclusions

Tether pulling experiments carried out with the magnetic tweezers demonstrated that the Crooks fluctuation theorem, previously verified experimentally at molecular level (single molecule experiments) is also valid at mesoscale level (single cell experiments). As predicted by the theory, driving a membrane tether system reversibly between two equilibrium states through non-equilibrium processes allows calculating the free energy between the two equilibrium states. The free energy does not depend on the intermediary states.

Crooks fluctuation theorem allows reconstructing the free energy profiles of membrane tethers as a function of their length. As ΔG turns to be proportional to Δx^2 , the tethers can be indeed modeled as springs: the result can be interpreted as the free energy of a system composed of N springs connected in parallel. Under this mechanical

analogy, the free energy profiles allow estimating Nk (the product between the average number of tethers pulled in an experiment and the spring constant). Remarkably, within the accuracy of our analysis, Nk is consistent with the value provided by the previous tether study, where the tether length as a function of time was fit with a phenomenological viscoelastic model.

Applications at sub-cellular level

Background and significance

The sub-cellular project, developed in collaboration with Dr. John Critser's group from the Cryobiology Laboratory, Department of Veterinary Pathobiology, UMC, involved measurements for the cytoskeleton viscoelastic parameters in mouse oocytes. The primary motivation of this work was to investigate the extent to which the cryopreservation process alters the cytoskeletal network in oocytes, preventing them from undergoing a successful development after *in vitro* fertilization. Surpassing its original goal, this project eventually suggested a procedure to increase the cryosurvival rate and developmental competence in frozen-thawed eggs.

In vitro fertilization represents not only a solution for millions of infertile couples [70], but also an essential tool for transgenic animal production [71], embryonic stem cell research and reproductive or therapeutic cloning [72]. For most mammalian species, the overall success of the method (taking into account the cryosurvival rate, the fertilization and the developmental competence of thawed oocytes) is very low; recent publications using human oocytes report developmental competence below 10% (1%, [73]; 5.6% [74]). Finding cryopreservation techniques that yield higher survival rates and better developmental competence represents a major challenge.

It is puzzling that cryopreservation, a process successfully mastered in most other cell types, does not work well in most oocytes. Among others, some important features of the oocytes might be responsible for their cryo-sensitivity:

1. **Size:** oocytes are huge cells (~100 μm in diameter). The cryoprotective agent does not physically diffuse in a 100-micron cell as easily as in a typical 10-micron somatic cell. A cell diameter 10x bigger corresponds to a cell volume 1000x bigger, with a surface/volume ratio 10x smaller!

2. **Structure:** unfertilized oocytes do not have a nucleus. They are arrested in the second metaphase of meiosis (MII), a cell division stage in which their chromosomes are arranged in a very specific architecture in their cytoplasm (lined up in the meiotic spindle). The lack of a protective nuclear membrane makes the chromosomes sensitive to any mechanical force, such as those associated with the ice crystal formation or osmotic volume changes in certain stages of cryopreservation.

3. **Number:** the number of mammalian oocytes that can be obtained during a single collection are far fewer ($\sim 1 \times 10^1$ to 1×10^2) than most other cell types typically cryopreserved such as spermatozoa (1×10^6 to 1×10^9) or red blood cells (1×10^7 - 1×10^{10}). In this regard, MII oocytes are unlike cell lines which can “survive” cryopreservation by simply compensating for low cryopreservation efficiencies via rapid cell division either *in vitro* (e.g., many immortalized cell lines) or *in vivo* (e.g., hematopoietic stem cells). Therefore oocyte cryopreservation has a crucial particularity: each individual cell matters.

Most cryoprotective techniques currently in use try to prevent cryoinjury (intracellular ice crystal formation, solute effects injury, or both) using equilibrium (e.g. slow cooling) or non-equilibrium (e.g. vitrification) cryopreservation methods [75, 76].

However, these approaches often lead to decreased cell viability that adversely affects the post-fertilization development of the zygote [77, 78].

The cytoskeletal network in mammalian oocytes has a particular organization of microtubules and microfilaments, as well as intermediate filaments [79, 80], all subject to alteration due to one or more of the steps in cryopreservation. Studies assessing the effects of cryopreservation on the oocyte cytoskeleton have provided limited information. Most have focused on the meiotic spindle [74, 81-83]. Nearly all of those aimed at studying microfilaments have been restricted to qualitative studies on the cortical actin band [84]. More global and quantitative characterization of the post-frozen cytoskeletal network *per se* has not been performed. Since microfilaments control a number of cellular functions [85] and post-fertilization events in oocytes [86], the sub-cellular project investigated the role of the overall actin network on the survival rate and developmental competence of cryopreserved mouse oocytes.

Cytoplasmic viscosity of human oocytes correlates with their developmental competence [87]. Studies performed on somatic cells show that intracellular viscoelastic properties are strongly affected by cytoskeletal integrity [88]. These observations suggest that intracellular viscoelastic parameters may provide a quantitative measure of cytoskeletal integrity, which, in turn, may reflect the developmental competence of oocytes.

Specific aims

1. Quantify alterations in the actin cytoskeletal network induced by cryopreservation by determining the intracellular viscoelastic characteristics of fresh and cryopreserved (frozen-thawed) oocytes.

2. Test the hypothesis that the reversible disassembly of the microfilament network prior to cryopreservation using an actin depolymerizing agent, such as LatA [89, 90] confers cryo-protection.

3. Verify the concept in somatic cells.

Experimental design

All chemicals were from the Sigma Aldrich chemical company (St Louis, MO) unless otherwise noted.

Oocyte collection and bead injection

Mouse oocytes were retrieved from super-ovulated CD-1 female mice and injected with 5-micron super-paramagnetic beads (Dynabeads M-500, Dynal ASA, Oslo, Norway), one bead/cell, from a stock solution containing 2×10^5 beads/ml in water (Fig. 26). After injection, oocytes were returned to TALP-Hepes and held until viscoelastic measurements were carried out. The oocyte collection and injection were carried out in the Critser Lab.

Experimental group assignment

Injected oocytes were randomly distributed into three experimental groups:

Group 1: fresh-control group - no treatment was applied.

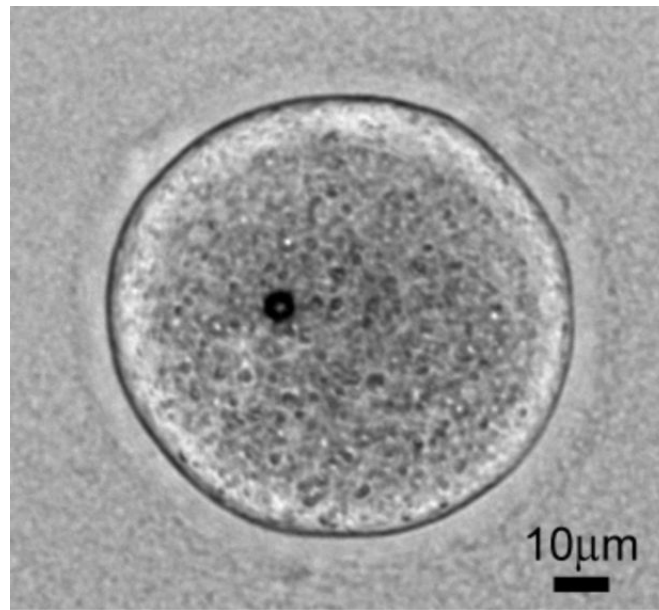


Figure 26. CD-1 mouse oocyte injected with a 5-micron paramagnetic bead.
Note the embedding fibrin gel.

Group 2: frozen-control group - cells were cryopreserved without LatA.

Group 3: frozen-LATA group - cells were incubated in 1 μM LatA (Molecular Probes, Eugene, OR) in TALP-Hepes for ~ 45 minutes at ~ 37 $^{\circ}\text{C}$ prior to cryopreservation. The LatA solution was prepared in TALP-Hepes by diluting a 100 μM stock solution in DMSO.

Groups 2 and 3 were cryopreserved in a TALP-Hepes solution containing DMSO (1 M), sucrose (0.2 M) and fetal bovine serum (10% v/v), supplemented with Lata (1 μM) for group 3, following a published protocol [91] with slight modifications, in the Critser Lab. Cells were kept frozen in liquid nitrogen for > 24 hours, then thawed. LatA was washed out in group 3. Thawed cells were injected with a magnetic bead after 1 h recovery time after thawing.

Magnetic tweezers experiments

Oocytes in each group were embedded in a fibrin gel to prevent their movement under the action of the magnetic force, as described below. In a typical experiment, one oocyte was placed on a triangular coverslip in 10 μl of 10 mg/ml bovine fibrinogen solution (in 0.15 M NaCl), then covered with mineral oil to prevent evaporation. The fibrinogen solution was then converted to fibrin gel by adding 1-2 μl of bovine thrombin solution (50 NIH units/ml). The gelation time was 1-2 minutes. The triangular coverslip, prepared by cutting 18 mm square No 1 $\frac{1}{2}$ coverslips (Corning Inc., Corning, NY) was placed in the removable sample holder, between the two poles of the magnetic tweezers [16]. Two-second constant force loads were applied to the cytoskeletal network through the injected magnetic bead. The magnetic force, which was constant along the entire bead

trajectory within an experiment, ranged from 22 to 280 pN across experiments. The cytoskeletal response was monitored through the movement of the bead using video-microscopy. All measurements were performed at locations ranging from 0 to $0.85R$ μm from the center of the cell, where R is the radius of the cell. Oocytes were kept at 37°C in TALP-Hepes until gel embedding. All measurements were performed at room temperature. A typical experiment lasted 3-5 minutes (including the gelation time).

Modeling and data analysis

Each bead trajectory was approximated as a sum of an exponential and a linear function of time:

$$x(t) = A \cdot (1 - e^{-Bt}) + C \cdot t \quad (12)$$

where x is bead displacement, t is time and A , B and C are fitting parameters. This model-independent approach provided τ , the relaxation time of the cytoplasm ($\tau = 1/B$), a universal intrinsic property of viscoelastic materials [92].

Each bead trajectory was also modeled with the simplest viscoelastic model (Fig. 27) which realistically described the cytoplasmic environment during creep ($F \neq 0$), as described in [10]. Each oocyte was characterized in terms of elastic and viscous parameters. The elastic (k) and friction (μ and μ_1) coefficients were determined by fitting the creep part of the bead displacement curve with the solution of the model:

$$x(t) = \frac{F}{k} \cdot \left[\frac{t}{\mu_1/k} + \left(1 - e^{-\frac{t}{\mu/k}} \right) \right] \quad (13)$$

where F is the magnetic force.

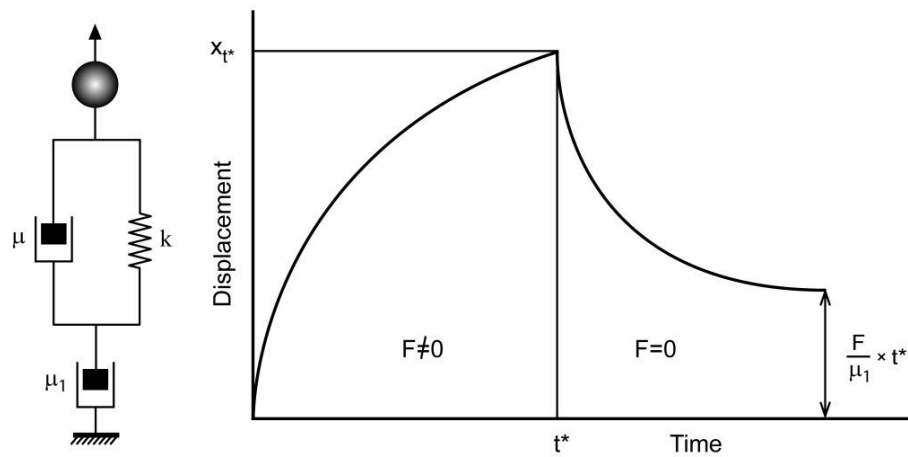


Figure 27. Viscoelastic model for the cytoplasmic environment.

Left. Phenomenological model composed of a Voigt body (k, μ) in series with a dashpot (μ_1). *Right.* The trajectory of the bead as given by the solution of the phenomenological model with during creep ($F \neq 0$) and relaxation ($F = 0$). F = magnetic force; k = elastic coefficient; μ and μ_1 = friction coefficients (see text for details)

Note that for large t ($\gg \mu/k$), $x(t)$ is determined by the combination of a constant spring-like (i.e. F/k) and viscous (i.e. Ft/μ_1) deformation, the latter characterized exclusively by the cytoskeletal component of cytoplasmic friction, μ_1 . For shorter times (i.e. $t < \mu/k$), $x(t)$ represents a mostly viscous displacement (proportional to $1/\mu + 1/\mu_1 \approx 1/\mu$), quantified in terms of both the cytoskeletal and liquid component of cytoplasmic friction (see below, under Discussion for the physical interpretation of μ and μ_1). Comparison of the two expressions for $x(t)$ leads to $\tau = \mu/k$. Similarly, the fitting parameters A and C can be identified respectively with $\frac{F}{k}$ and $\frac{F}{\mu_1}$. The friction parameters (μ and μ_1) can be converted into cytoplasmic viscosity (η and η_1) according to the Stokes formula $\eta = \mu/(6\pi R)$, where R is the radius of the bead.

Since it has recently been noted that the mechanical behavior of living cells shows time-scale invariance [93, 94], we also fit the creep using a power law: $j(t) = A(t/t_0)^\alpha$. Here j is the compliance (bead displacement normalized for force), $t_0 = 1$ s and A and α are fitting parameters [93, 94].

The quantitative results obtained for the viscoelastic parameters k , μ and μ_1 in groups 2 and 3 were compared with those for the control group 1 using a standard t-test in SAS Statistical Software (SAS Institute Inc., Cary, NC). The relaxation time τ , which showed a log-normal distribution, was compared across groups using a non-parametric test (Kolmogorov-Smirnov).

Proof of concept on somatic cells

CHO cells purchased from American Type Culture Collection (Manassas, VA) were grown at 37°C in 5% CO₂ in DMEM (Invitrogen Corp., Carlsbad, CA) containing 10% FBS (U.S. Bio-Technologies, Pottstown, PA), 10 µg/ml penicillin, streptomycin, gentamicin and kanamycin sulphate (Invitrogen Corp., Carlsbad, CA).

Cells were distributed in 7 experimental groups:

Group 1 (control): cells were frozen in a freezing medium containing 1.5 M DMSO in FBS.

Group 2 (no cryoprotectant, no LatA): cells were frozen in FBS.

Group 3 (no cryoprotectant, LatA 0.2 µM in FBS): cells were frozen in a freezing medium containing 0.2 µM LatA in FBS.

Group 4 (no cryoprotectant, LatA 0.5 µM in FBS): cells were frozen in a freezing medium containing 0.5 µM LatA in FBS.

Group 5 (no cryoprotectant, LatA 1 µM in FBS): cells were frozen in a freezing medium containing 1 µM LatA in FBS.

Group 6 (no cryoprotectant, LatA 2 µM in FBS): cells were frozen in a freezing medium containing 2 µM LatA in FBS.

Group 7 (DMSO 1.5 M, LatA 1 µM in FBS): cells were frozen in a freezing medium containing 1.5 M DMSO, 1 µM LatA in FBS.

In each group, cells were kept in their corresponding freezing medium for 30 min prior to commencing the cooling process. Cells were frozen at the same time, kept 24 h in

liquid nitrogen then thawed and cultured in Petri dishes. Cells in each group were counted in a haemocytometric chamber before freezing and 24 h after thawing. Before resuspending the cells for counting, the cultures were washed twice with PBS to remove the non-attached cells.

The cryosurvival rate was calculated as follows. Assuming a similar doubling time (τ) in each group, the number of surviving cells after thawing is:

$$N_B = N_c / 2^{t/\tau} \quad (14)$$

where N_c is the number of cells at t hours (24, in this case) after thawing (as counted in the haemocytometric chamber).

In each group, the cryosurvival rate is N_B / N_A , where N_A is the number of cells before freezing (as counted in the haemocytometric chamber).

Results

Magnetic bead movement through the intracellular environment

The viscoelastic properties of fresh and cryopreserved oocytes were determined by fitting the intracellular trajectory of the magnetic bead using (1) a model of linear viscoelasticity [63] and (2) a power law function [93, 95]. Results in Fig. 28 show that both approaches provide an excellent description of bead movement. The power law form reflects the known characteristics of viscoelastic materials: they possess a spectrum of relaxation times. The fact that the adapted model of linear viscoelasticity provided similarly good results suggests that this spectrum is dominated by one (*i.e.* largest) τ value. Numerical results are summarized in Table 2.

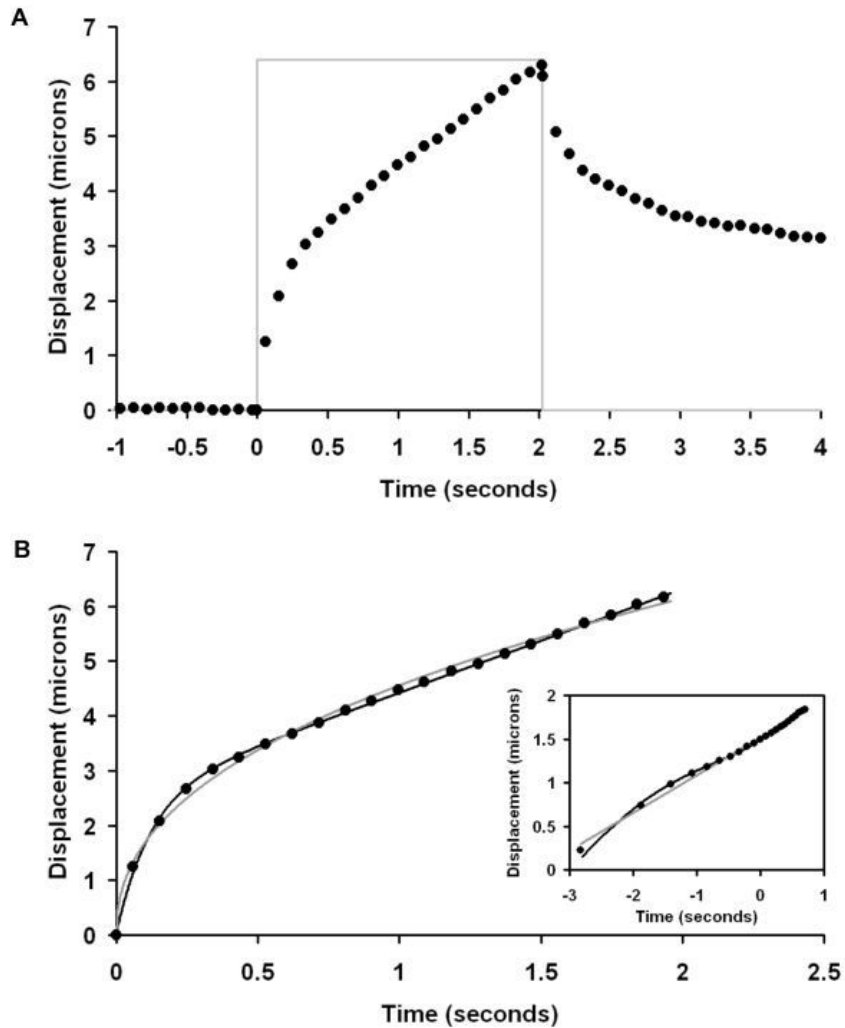


Figure 28. Typical bead trajectory under a 2-second constant force pulse. *Upper panel.* Experimental data (filled circles: bead position; gray line: magnetic pulse; “0” on the time axis represents the moment when the force pulse was applied). *Lower panel.* Best fit to the trajectory during creep (filled circles: experimental data points; black line: best fit with the linear viscoelastic model; gray line: best fit with the power law). Inset: bead trajectory on a log-log scale (the numbers along both axis are powers of e , the base of natural logarithm).

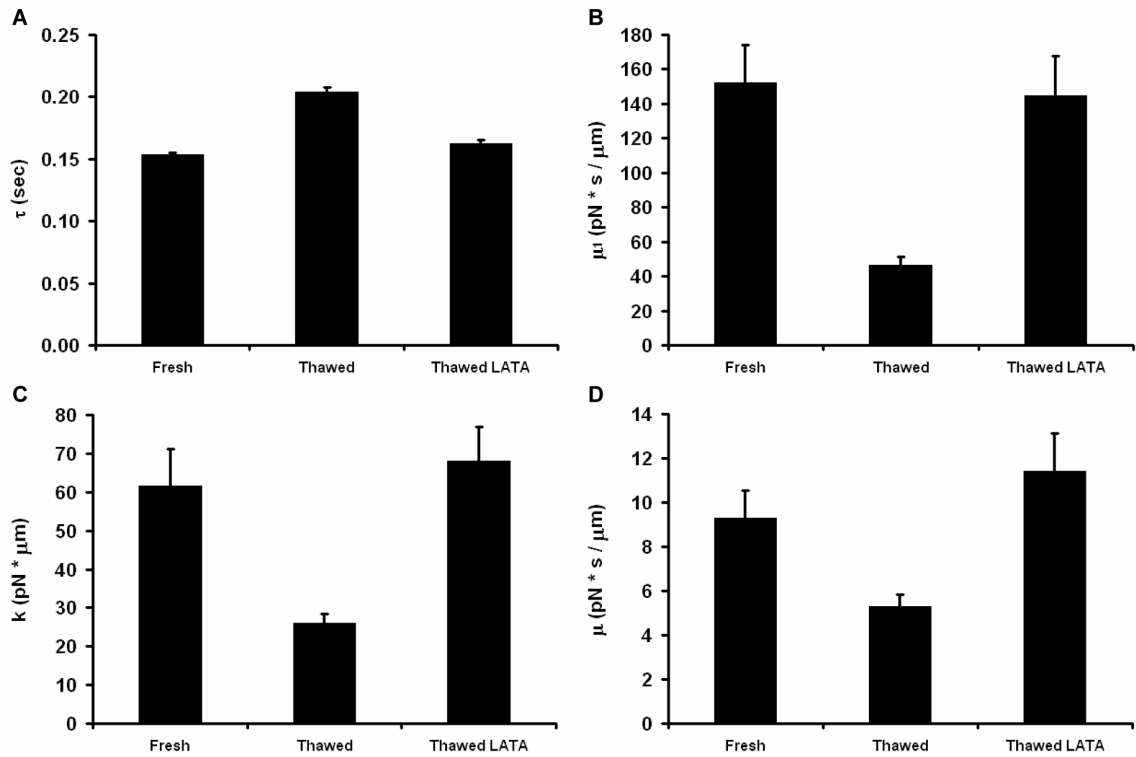


Figure 29. Results: viscoelastic parameters in all experimental groups.

Viscoelastic parameters before (Fresh, group 1; non-frozen control, $n = 29$ cells) and after freezing, without (Thawed, group 2; frozen-thawed control, $n = 16$ cells) and with (Thawed-LATA, group 3; $n = 19$ cells) LatA pretreatment. (A) Relaxation time. (B) Friction coefficient μ_1 . (C) Elastic coefficient k . (D) Friction coefficient μ . All parameters show a significant statistical difference (see p values in Table 1) between groups 1 and 2. There is no significant statistical difference between groups 1 and 3. Bars represent geometric mean \pm geometric SE (panel A) and mean \pm SEM (panels B, C and D).

Table 2. Quantitative results in oocyte cytoskeleton study.

	Group 1 Fresh untreated	Group 2 Thawed untreated	Group 3 Thawed LATA
τ (sec; geometric mean \pm geometric SE)	0.153 \pm 0.001	0.204 \pm 0.004*	0.162 \pm 0.003
k (pN $\times\mu$ m; mean \pm SEM)	61.6 \pm 9.4	25.7 \pm 2.5*	68.6 \pm 8.7
μ (pN \times s/ μ m, mean \pm SEM)	9.2 \pm 1.2	5.3 \pm 0.5*	11.4 \pm 1.7
μ_1 (pN \times s/ μ m, mean \pm SEM)	152.4 \pm 21.5	46.2 \pm 5.2†	144.5 \pm 22.9
α (mean \pm SEM)	0.362 \pm 0.01	0.471 \pm 0.02†	0.417 \pm 0.18
A (μ m/pN, geometric mean \pm geometric SE)	0.028 \pm 0.001	0.056 \pm 0.003†	0.027 \pm 0.001

* $p < 0.05$

† $p < 0.01$

Effect of cryopreservation on intracellular viscoelastic properties

As the results in Table 2 and Fig. 29 indicate, freezing of oocytes leads to marked changes in material properties, in particular to the increase of the relaxation time τ . Larger τ suggests a more rigid, less responsive and adaptive cytoskeleton. Furthermore, the other viscoelastic parameters (μ , μ_1 , k) were significantly smaller in group 2 than in group 1.

Effect of LatA pretreatment on intracellular viscoelastic properties in thawed oocytes

The relaxation time in the frozen-thawed LATA pre-treated group (group 3) was not statistically different from the one in group 1 (Table 1 and Fig. 29). Similarly, μ , μ_1 and k (as well as the power law parameters) were not significantly different between groups 1 and 3 (Table 1 and Fig 30 B-D). *In vitro* fertilization and developmental competence assays carried out in Critser Lab showed that LatA pretreatment improved not only the cryosurvival rate (with 20%) but also the developmental competence in cryopreserved oocytes (nearly twice as many cells reached the blastocyst stage in LatA Group; data not shown).

Effect of LatA pretreatment on somatic cell cryopreservation

Results normalized for the control (Group 1) are shown in Fig. 30. LatA treatment, in the absence of any other cryoprotective agent increased the cryosurvival rate. The number of survivors increased with the concentration of LATA. While FBS alone (group 2, no DMSO, no LATA) provided almost no survivors, the 2 μ M LATA group provided at least as many survivors as DMSO 1.5 M alone.

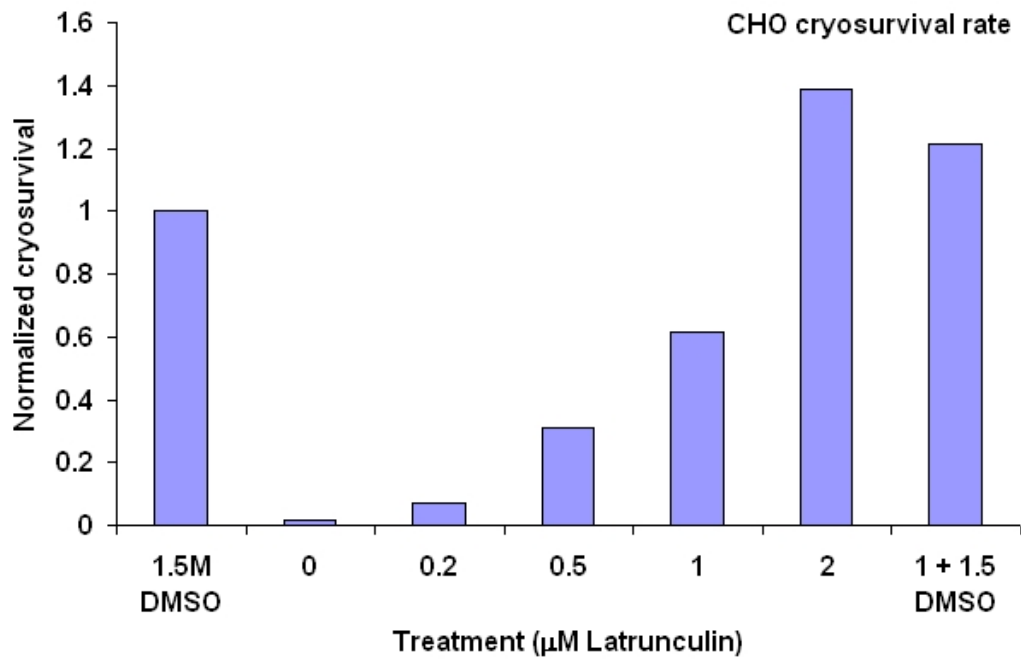


Figure 30. Proof of concept in somatic cells.

Cryosurvival rate in CHO cells with DMSO alone (left bar), DMSO + 1 μM Latrunculin A (right bar) and Latrunculin A solutions in concentrations ranging from 0 to 2 μM , without DMSO.

This result demonstrates that LATA, alone or in combination with other agents can be successfully used as a cryoprotectant in somatic cells.

Discussion

The first aim of this study was to demonstrate and quantify the cytoskeletal alteration induced by cryopreservation. The second aim was to test the hypothesis that cryopreservation, in the absence of a microfilament network, causes less damage to the cell than in its presence. Thus, the F actin network of mouse oocytes was reversibly dismantled prior to their freezing. The efficacy of this method was assessed by quantitative measurements of intracellular viscoelastic properties. Viscoelasticity measurements were carried out using a magnetic tweezers: magnetic beads injected into oocytes were displaced under controlled force and their trajectory was recorded. Viscoelastic parameters were determined by modeling these trajectories with a standard model of viscoelasticity.

The characterization of the physical properties of the cytoplasmic environment through the displacement of magnetic beads is a powerful method with a long history [1, 3, 5, 10, 11, 21, 96]. The reported numerical values of the viscoelastic parameters show a strong dependence on cell type and the specific method used. The present results for fresh mouse oocytes are much closer to those found in sea urchin eggs [10] than to those in various somatic cells [3, 5, 11, 96].

The results from our quantitative study were interpreted in terms of three characteristic cytoplasmic quantities (Fig. 27): the cytoskeletal (μ_1) and liquid (μ) friction constants and an elastic coefficient (k). As the bead starts moving, it commences

to locally deform the cytoskeleton. This elastic deformation continues until $t \approx \tau$, where the time scale $\tau = \mu/k$ (another characteristic cytoplasmic quantity) is determined by both the viscous and elastic properties of the environment. During this time, bead displacement (proportional to $1/\mu + 1/\mu_1$) is dominated by the liquid component of cytoplasmic viscosity ($1/\mu + 1/\mu_1 \approx 1/\mu$; Table 1). The origin of μ is mostly in the viscous liquid properties of the cytoplasm (for fresh oocytes, the associated viscosity $\eta \approx 10 \text{ Pa} \times \text{s}$, is ~ 100 times larger than that of water), whereas the origin of k is the elasticity of the cytoskeletal filaments. Once the cytoskeletal mesh is locally maximally stretched (*i.e.* $t > \mu/k$), the bead's total displacement is dominated by the combination of this stretch (*i.e.* F/k) and the deformation due to the viscous properties of the oocyte cytoskeleton, whose origin is in the breakage of cross-links between the bead and the mesh [21].

Cryopreservation in the absence of LatA treatment (group 2) resulted in an increase of the relaxation time and a reduction of all three viscoelastic parameters (Table 2 and Fig. 29). This finding is consistent with the interpretation of these quantities given above. If the freeze-thaw process indeed leads to the fragmentation of the cytoskeleton and thus to loss of the extent of its interconnectedness, then both its viscous and elastic characteristics are expected to be diminished. LatA pre-treatment reversed this trend: the three viscoelastic constants and the relaxation time do not significantly differ from their corresponding values for fresh oocytes (Table 2 and Fig. 29). Even though both cryopreservation and LatA treatment alone induce the disruption of the cytoskeletal network, the two mechanisms are quite different. First, in the former case *a priori* all

components of the cytoskeleton are affected, whereas in the second case only the F actin assembly is altered. Second, changes in cytoplasmic viscoelastic properties are mostly irreversible upon cryopreservation, whereas they are reversible following LatA treatment. These results support the hypothesis that the effect of cryopreservation on the F actin mesh is much more critical than on the collection of G actin molecules. A possible explanation is that freezing renders the microfilaments brittle and thus makes them unable to recover their physiological viscoelasticity. Removal of LatA, on the other hand, allows the formation of a *de novo* microfilament network with no memory of cryopreservation. Furthermore, these findings also suggest that, at least in the mouse model, the effect of freezing is more dramatic on the actin mesh than on the other components of the cytoskeleton.

Microfilaments play a significant role in oocyte maturation and fertilization events [97]. Qualitative studies focusing on the cortical microfilaments have shown that factors associated with cryopreservation (e.g. exposure to the cryoprotectant) can cause disruption of the microfilament network in mammalian oocytes (reviewed in [98]), the magnitude of the effect depending on the particular cryoprotective agent used, or species from which the oocyte is derived [84, 99-101]. One particular organelle strongly associated with the microfilament network (through the cortical actin mesh) is the plasma membrane. If these two structures are differentially affected by freezing, the former (due to its decreased elasticity) may impose increased stress on the latter and possibly cause permanent damage in its structure. This is supported by the findings in [102] where the effect of cryopreservation on the cytoskeleton and early post-fertilization events in mouse oocytes were investigated. Ref. [84] showed that neither the cortical actin band nor

cytoplasmic microfilaments of bovine oocytes could recover from the damage caused by cryopreservation, despite extensive post-thaw incubation.

Exposure to LatA could prevent stress from being transmitted to and from the membrane through the actin network. As a result, the membrane may become more flexible and better tolerate the osmotic imbalance arising in the course of freezing and thawing. Conversely, intracellular structures would be exposed less to stress caused by membrane tension variations.

This is the first quantitative study to assess the effects of cryopreservation on microfilaments in mature oocytes. It shows that freezing/thawing results in significant changes in cytoplasmic viscoelastic properties, which do not appear to be fully reversible by post-thaw incubation in culture. It also shows that reversible depolymerization of the actin network prior to cryopreservation largely preserves physiological viscoelasticity. Filamentous actin interacts with the other major cytoskeletal components [103] (*i.e.* intermediate filaments [104], microtubules [105]); therefore, these structures may also be affected by LatA treatment. The quantitative data thus suggest that upon the regeneration of the microfilament network, the other cytoskeletal components also regain their physiological structure. This observation implies that LatA treatment confers a protective effect and leads to considerable improvement in the survival rate and developmental competence of frozen-thawed mouse oocytes, pointing to a new role for LatA as a cryoprotective agent.

References

1. Crick , F. and A. Hughes, *The physical properties of the cytoplasm: a study by means of the magnetic particle method*. Exp. Cell. Res., 1949. **1**: p. 37-80.
2. Strick, T.R., et al., *Behavior of supercoiled DNA*. Biophys J, 1998. **74**(4): p. 2016-28.
3. Valberg, P.A. and D.F. Albertini, *Cytoplasmic motions, rheology, and structure probed by a novel magnetic particle method*. J Cell Biol, 1985. **101**(1): p. 130-40.
4. Moller, W., et al., *Probing mechanical properties of living cells by magnetopneumography*. J Aerosol Med, 1997. **10**(3): p. 173-86.
5. Moller, W., et al., *Magnetic phagosome motion in J774A.1 macrophages: influence of cytoskeletal drugs*. Biophys J, 2000. **79**(2): p. 720-30.
6. Dessinges, M.N., et al., *Single-molecule assay reveals strand switching and enhanced processivity of UvrD*. Proc Natl Acad Sci U S A, 2004. **101**(17): p. 6439-44.
7. Danilowicz, C., et al., *DNA unzipped under a constant force exhibits multiple metastable intermediates*. Proc Natl Acad Sci U S A, 2003. **100**(4): p. 1694-9.
8. Kuznetsov, O.A. and K.H. Hasenstein, *Magnetophoretic induction of curvature in coleoptiles and hypocotyls*. J Exp Bot, 1997. **48**(316): p. 1951-7.
9. Hiramoto, Y., *Mechanical properties of the protoplasm of the sea urchin egg. II. Fertilized egg*. Exp Cell Res, 1969. **56**(2): p. 209-18.

10. Hiramoto, Y., *Mechanical properties of the protoplasm of the sea urchin egg. I. Unfertilized egg.* Exp Cell Res, 1969. **56**(2): p. 201-8.
11. Bausch, A.R., W. Moller, and E. Sackmann, *Measurement of local viscoelasticity and forces in living cells by magnetic tweezers.* Biophys J, 1999. **76**(1 Pt 1): p. 573-9.
12. Bausch, A.R., et al., *Rapid stiffening of integrin receptor-actin linkages in endothelial cells stimulated with thrombin: a magnetic bead microrheology study.* Biophys J, 2001. **80**(6): p. 2649-57.
13. Bausch, A.R., et al., *Local measurements of viscoelastic parameters of adherent cell surfaces by magnetic bead microrheometry.* Biophys J, 1998. **75**(4): p. 2038-49.
14. Barbic, M., et al., *Scanning probe electromagnetic tweezers.* Applied Physics Letters, 2001. **79**(12): p. 1897-1899.
15. Dichtl, M.A. and E. Sackmann, *Microrheometry of semiflexible actin networks through enforced single-filament reptation: frictional coupling and heterogeneities in entangled networks.* Proc Natl Acad Sci U S A, 2002. **99**(10): p. 6533-8.
16. Hosu, B.G., et al., *Magnetic tweezers for intracellular applications.* Review of Scientific Instruments, 2003. **74**(9): p. 4158-4163.
17. Amblard, F., et al., *Subdiffusion and Anomalous Local Viscoelasticity in Actin Networks.* Physical Review Letters, 1996. **77**(21): p. 4470-4473.
18. Haber, C. and D. Wirtz, *Magnetic tweezers for DNA micromanipulation.* REVIEW OF SCIENTIFIC INSTRUMENTS, 2000. **71**(12): p. 4561-4570.
19. Gosse, C. and V. Croquette, *Magnetic tweezers: micromanipulation and force measurement at the molecular level.* Biophys J, 2002. **82**(6): p. 3314-29.
20. Huang, H., et al., *Three-dimensional cellular deformation analysis with a two-photon magnetic manipulator workstation.* Biophys J, 2002. **82**(4): p. 2211-23.

21. de Vries, A.H., et al., *Micro magnetic tweezers for nanomanipulation inside live cells*. Biophys J, 2005. **88**(3): p. 2137-44.
22. Soule, D.E., C.W. Nezbeda, and A.W. Czanderna, Rev. Sci. Instr., 1964. **35**: p. 1504
23. Collin, D., et al., *Verification of the Crooks fluctuation theorem and recovery of RNA folding free energies*. Nature, 2005. **437**(7056): p. 231-4.
24. Schmidtke, D. and S. Diamond, *Direct observation of membrane tethers formed during neutrophil attachment to platelets or P-selectin under physiological flow*. JOURNAL OF CELL BIOLOGY, 2000. **149**(3): p. 719-729.
25. Ramachandran, V., et al., *Dynamic alterations of membrane tethers stabilize leukocyte rolling on P-selectin*. Proc Natl Acad Sci U S A, 2004. **101**(37): p. 13519-24.
26. Alon, R., et al., *The kinetics and shear threshold of transient and rolling interactions of L-selectin with its ligand on leukocytes*. Proc Natl Acad Sci U S A, 1998. **95**(20): p. 11631-6.
27. McCarty, O.J., et al., *Immobilized platelets support human colon carcinoma cell tethering, rolling, and firm adhesion under dynamic flow conditions*. Blood, 2000. **96**(5): p. 1789-97.
28. Rustom, A., et al., *Nanotubular highways for intercellular organelle transport*. Science, 2004. **303**(5660): p. 1007-10.
29. Vidulescu, C., S. Clejan, and C. O'Connor K, *Vesicle traffic through intercellular bridges in DU 145 human prostate cancer cells*. J Cell Mol Med, 2004. **8**(3): p. 388-96.
30. Polishchuk, E.V., et al., *Mechanism of constitutive export from the golgi: bulk flow via the formation, protrusion, and en bloc cleavage of large trans-golgi network tubular domains*. Mol Biol Cell, 2003. **14**(11): p. 4470-85.
31. White, J., et al., *Rab6 coordinates a novel Golgi to ER retrograde transport pathway in live cells*. J Cell Biol, 1999. **147**(4): p. 743-60.

32. Upadhyaya, A. and M.P. Sheetz, *Tension in tubulovesicular networks of Golgi and endoplasmic reticulum membranes*. Biophys J, 2004. **86**(5): p. 2923-8.
33. Giuffre, L., et al., *Monocyte adhesion to activated aortic endothelium: role of L-selectin and heparan sulfate proteoglycans*. J Cell Biol, 1997. **136**(4): p. 945-56.
34. Sheetz, M.P., *Cellular plasma membrane domains*. Mol Membr Biol, 1995. **12**(1): p. 89-91.
35. Roux, A., et al., *A minimal system allowing tubulation with molecular motors pulling on giant liposomes*. Proc Natl Acad Sci U S A, 2002. **99**(8): p. 5394-9.
36. Leduc, C., et al., *Cooperative extraction of membrane nanotubes by molecular motors*. Proc Natl Acad Sci U S A, 2004. **101**(49): p. 17096-101.
37. Koster, G., et al., *Membrane tube formation from giant vesicles by dynamic association of motor proteins*. Proc Natl Acad Sci U S A, 2003. **100**(26): p. 15583-8.
38. Waugh, R.E. and R.M. Hochmuth, *Mechanical equilibrium of thick, hollow, liquid membrane cylinders*. Biophys J, 1987. **52**(3): p. 391-400.
39. Bo, L. and R.E. Waugh, *Determination of bilayer membrane bending stiffness by tether formation from giant, thin-walled vesicles*. Biophys J, 1989. **55**(3): p. 509-17.
40. Waugh, R.E., et al., *Local and nonlocal curvature elasticity in bilayer membranes by tether formation from lecithin vesicles*. Biophys J, 1992. **61**(4): p. 974-82.
41. Derenyi, I., F. Julicher, and J. Prost, *Formation and interaction of membrane tubes*. Phys Rev Lett, 2002. **88**(23): p. 238101.
42. Cuvelier, D., et al., *Coalescence of membrane tethers: experiments, theory, and applications*. Biophys J, 2005. **88**(4): p. 2714-26.
43. Koster, G., et al., *Force barriers for membrane tube formation*. Phys Rev Lett, 2005. **94**(6): p. 068101.

44. Sheetz, M.P., *Cell control by membrane-cytoskeleton adhesion*. Nat Rev Mol Cell Biol, 2001. **2**(5): p. 392-6.
45. Dai, J. and M.P. Sheetz, *Membrane tether formation from blebbing cells*. Biophys J, 1999. **77**(6): p. 3363-70.
46. Shao, J.Y., H.P. Ting-Beall, and R.M. Hochmuth, *Static and dynamic lengths of neutrophil microvilli*. Proc Natl Acad Sci U S A, 1998. **95**(12): p. 6797-802.
47. Hochmuth, R.M., et al., *Extensional flow of erythrocyte membrane from cell body to elastic tether. II. Experiment*. Biophys J, 1982. **39**(1): p. 83-9.
48. Shao, J.Y. and J. Xu, *A modified micropipette aspiration technique and its application to tether formation from human neutrophils*. J Biomech Eng, 2002. **124**(4): p. 388-96.
49. Zhelev, D.V. and R.M. Hochmuth, *Mechanically stimulated cytoskeleton rearrangement and cortical contraction in human neutrophils*. Biophys J, 1995. **68**(5): p. 2004-14.
50. Dai, J., et al., *Membrane tension in swelling and shrinking molluscan neurons*. J Neurosci, 1998. **18**(17): p. 6681-92.
51. Raucher, D. and M.P. Sheetz, *Characteristics of a membrane reservoir buffering membrane tension*. Biophys J, 1999. **77**(4): p. 1992-2002.
52. Girdhar, G. and J.Y. Shao, *Membrane tether extraction from human umbilical vein endothelial cells and its implication in leukocyte rolling*. Biophys J, 2004. **87**(5): p. 3561-8.
53. Dai, J. and M.P. Sheetz, *Mechanical properties of neuronal growth cone membranes studied by tether formation with laser optical tweezers*. Biophys J, 1995. **68**(3): p. 988-96.
54. Inaba, T., et al., *Formation and maintenance of tubular membrane projections require mechanical force, but their elongation and shortening do not require additional force*. J Mol Biol, 2005. **348**(2): p. 325-33.

55. Titushkin, I. and M. Cho, *Distinct membrane mechanical properties of human mesenchymal stem cells determined using laser optical tweezers*. Biophys J, 2006. **90**(7): p. 2582-91.
56. Heinrich, V. and R.E. Waugh, *A piconewton force transducer and its application to measurement of the bending stiffness of phospholipid membranes*. Ann Biomed Eng, 1996. **24**(5): p. 595-605.
57. Shao, J.Y. and R.M. Hochmuth, *Micropipette suction for measuring piconewton forces of adhesion and tether formation from neutrophil membranes*. Biophys J, 1996. **71**(5): p. 2892-901.
58. Marcus, W.D. and R.M. Hochmuth, *Experimental studies of membrane tethers formed from human neutrophils*. Ann Biomed Eng, 2002. **30**(10): p. 1273-80.
59. Sun, M., et al., *Multiple membrane tethers probed by atomic force microscopy*. Biophys J, 2005. **89**(6): p. 4320-9.
60. Xu, G. and J.Y. Shao, *Double tether extraction from human neutrophils and its comparison with CD4+ T-lymphocytes*. Biophys J, 2005. **88**(1): p. 661-9.
61. Girdhar, G., Y. Chen, and J.Y. Shao, *Double-tether extraction from human umbilical vein and dermal microvascular endothelial cells*. Biophys J, 2007. **92**(3): p. 1035-45.
62. Hegedus, B., et al., *Locomotion and proliferation of glioblastoma cells in vitro: statistical evaluation of videomicroscopic observations*. J Neurosurg, 2000. **92**(3): p. 428-34.
63. Fung, Y.C., *Biomechanics : mechanical properties of living tissues*. 2nd ed. 1993, New York: Springer-Verlag. xviii, 568 p.
64. Hochmuth, F.M., et al., *Deformation and flow of membrane into tethers extracted from neuronal growth cones*. Biophys J, 1996. **70**(1): p. 358-69.
65. Waugh, R.E. and R.G. Bauserman, *Physical measurements of bilayer-skeletal separation forces*. Ann Biomed Eng, 1995. **23**(3): p. 308-21.

66. Kerrigan, M.J., et al., *Regulatory volume increase (RVI) by in situ and isolated bovine articular chondrocytes*. J Cell Physiol, 2006. **209**(2): p. 481-92.
67. Bustamante, M., et al., *Regulatory volume increase is associated with p38 kinase-dependent actin cytoskeleton remodeling in rat kidney MTAL*. Am J Physiol Renal Physiol, 2003. **285**(2): p. F336-47.
68. Crooks, G.E., *Entropy production fluctuation theorem and the nonequilibrium work relation for free energy differences*. Phys Rev E Stat Phys Plasmas Fluids Relat Interdiscip Topics, 1999. **60**(3): p. 2721-6.
69. Kosztin, I., B. Barz, and L. Janosi, *Calculating potentials of mean force and diffusion coefficients from nonequilibrium processes without Jarzynski's equality*. J Chem Phys, 2006. **124**(6): p. 64106.
70. De Jonge, C.J. and C.L.R. Barratt, eds. *Assisted reproductive technology*. 2002, Cambridge University Press: Cambridge. 431.
71. Prather, R.S., et al., *Transgenic swine for biomedicine and agriculture*. Theriogenology, 2003. **59**(1): p. 115-123.
72. Wilmut, I., L. Young, and K.H. Campbell, *Embryonic and somatic cell cloning*. Reprod Fertil Dev, 1998. **10**(7-8): p. 639-43.
73. Mandelbaum, J., et al., *Cryopreservation in human assisted reproduction is now routine for embryos but remains a research procedure for oocytes*. Hum Reprod, 1998. **13 Suppl 3**: p. 161-74;discussion175-7.
74. Cobo, A., et al., *Use of fluorescence in situ hybridization to assess the chromosomal status of embryos obtained from cryopreserved oocytes*. Fertil Steril, 2001. **75**(2): p. 354-60.
75. Karow, A.M. and J.K. Critser, *Reproductive tissue banking : scientific principles*. 1997, San Diego: Academic Press. xviii, 472 p.
76. Woods, E.J., et al., *Fundamental cryobiology of reproductive cells and tissues*. Cryobiology, 2004. **48**(2): p. 146-56.

77. Fuku, E.J., J. Liu, and B.R. Downey, *In vitro viability and ultrastructural changes in bovine oocytes treated with a vitrification solution*. Mol Reprod Dev, 1995. **40**(2): p. 177-85.
78. Van Blerkom, J., *Maturation at high frequency of germinal-vesicle-stage mouse oocytes after cryopreservation: alterations in cytoplasmic, nuclear, nucleolar and chromosomal structure and organization associated with vitrification*. Hum Reprod, 1989. **4**(8): p. 883-98.
79. Gallicano, G.I., et al., *Novel cytoskeletal elements in mammalian eggs are composed of a unique arrangement of intermediate filaments*. Mech Dev, 1994. **45**(3): p. 211-26.
80. Grudzinskas, J.G. and J. Yovich, *Gametes : the oocyte*. 1995, Cambridge ; New York, NY, USA ;: Cambridge University Press. xiii, 441 p.
81. Bernard, A. and B.J. Fuller, *Cryopreservation of human oocytes: a review of current problems and perspectives*. Hum Reprod Update, 1996. **2**(3): p. 193-207.
82. Park, S.E., et al., *Cryopreservation of ICR mouse oocytes: improved post-thawed preimplantation development after vitrification using Taxol, a cytoskeleton stabilizer*. Fertil Steril, 2001. **75**(6): p. 1177-84.
83. Pickering, S.J., et al., *Transient cooling to room temperature can cause irreversible disruption of the meiotic spindle in the human oocyte*. Fertil Steril, 1990. **54**(1): p. 102-8.
84. Saunders, K.M. and J.E. Parks, *Effects of cryopreservation procedures on the cytology and fertilization rate of in vitro-matured bovine oocytes*. Biol Reprod, 1999. **61**(1): p. 178-87.
85. Lenart, P., et al., *A contractile nuclear actin network drives chromosome congression in oocytes*. Nature, 2005. **436**(7052): p. 812-818.
86. Schatten, G., et al., *Latrunculin inhibits the microfilament-mediated processes during fertilization, cleavage and early development in sea urchins and mice*. Exp Cell Res, 1986. **166**(1): p. 191-208.

87. Ebner, T., et al., *Developmental competence of oocytes showing increased cytoplasmic viscosity*. Hum Reprod, 2003. **18**(6): p. 1294-8.
88. Guilak, F., G.R. Erickson, and H.P. Ting-Beall, *The effects of osmotic stress on the viscoelastic and physical properties of articular chondrocytes*. Biophys J, 2002. **82**(2): p. 720-7.
89. Spector, I., et al., *Latrunculins--novel marine macrolides that disrupt microfilament organization and affect cell growth: I. Comparison with cytochalasin D*. Cell Motil Cytoskeleton, 1989. **13**(3): p. 127-44.
90. Spector, I., et al., *Latrunculins: novel marine toxins that disrupt microfilament organization in cultured cells*. Science, 1983. **219**(4584): p. 493-5.
91. Karlsson, J.O., et al., *Fertilization and development of mouse oocytes cryopreserved using a theoretically optimized protocol*. Hum Reprod, 1996. **11**(6): p. 1296-305.
92. Shaw, T., et al., *Commonality of elastic relaxation times in biofilms*. Phys Rev Lett, 2004. **93**(9): p. 098102.
93. Fabry, B., et al., *Time scale and other invariants of integrative mechanical behavior in living cells*. Physical Review E, 2003. **68**(4): p. -.
94. Lenormand, G., et al., *Linearity and time-scale invariance of the creep function in living cells*. J. R. Soc. Interface, 2004. **1**: p. 91-97.
95. Bursac, P., et al., *Cytoskeletal remodelling and slow dynamics in the living cell*. Nat Mater, 2005. **4**(7): p. 557-61.
96. Feneberg, W., M. Westphal, and E. Sackmann, *Dictyostelium cells' cytoplasm as an active viscoplastic body*. European Biophysics Journal with Biophysics Letters, 2001. **30**(4): p. 284-294.
97. Simerly, C., et al., *Cytoskeletal organization and dynamics in mammalian oocytes during maturation and fertilization*, in *Gametes - The Oocyte*, J.G. Grudzinskas and J.L. Yovich, Editors. 1995, Cambridge University Press: Cambridge. p. 54-94.

98. Vincent, C. and M.H. Johnson, *Cooling, cryoprotectants, and the cytoskeleton of the mammalian oocyte*. Oxf Rev Reprod Biol, 1992. **14**: p. 73-100.
99. Hotamisligil, S., M. Toner, and R.D. Powers, *Changes in membrane integrity, cytoskeletal structure, and developmental potential of murine oocytes after vitrification in ethylene glycol*. Biol Reprod, 1996. **55**(1): p. 161-8.
100. Vincent, C., et al., *Solvent effects on cytoskeletal organization and in-vivo survival after freezing of rabbit oocytes*. J Reprod Fertil, 1989. **87**(2): p. 809-20.
101. Vincent, C., et al., *Dimethylsulphoxide affects the organisation of microfilaments in the mouse oocyte*. Mol Reprod Dev, 1990. **26**(3): p. 227-35.
102. Eroglu, A., T.L. Toth, and M. Toner, *Alterations of the cytoskeleton and polyploidy induced by cryopreservation of metaphase II mouse oocytes*. Fertil Steril, 1998. **69**(5): p. 944-57.
103. Janmey, P.A., *The cytoskeleton and cell signaling: component localization and mechanical coupling*. Physiol Rev, 1998. **78**(3): p. 763-81.
104. Svitkina, T.M., A.B. Verkhovsky, and G.G. Borisy, *Plectin sidearms mediate interaction of intermediate filaments with microtubules and other components of the cytoskeleton*. J Cell Biol, 1996. **135**(4): p. 991-1007.
105. Pollard, T.D., S.C. Selden, and P. Maupin, *Interaction of actin filaments with microtubules*. J Cell Biol, 1984. **99**(1 Pt 2): p. 33s-37s.

VITA

Basarab G. Hosu was born on May 4th, 1968 and grew up in Bucharest, Romania. Following his passion for electronics, he enrolled “Spiru Haret” high school in Bucharest, specialized at that time in Electronics for Automation. As a high-school student, he won a few awards at local and national Electronics competitions. After a 3+ year career as an Electronics technician in a local research institute, he entered the Medical School at “Carol Davila” University (Bucharest, Romania), which he graduated in 1996. He practiced as a general pediatrician for 3 years, then returned to school and earned a MS degree in Biophysics under the guidance of Dr. Eugenia Kovacs (2001, “Carol Davila” University).

In 2002 he started the PhD program in Biological Sciences/Biophysics at the University of Missouri-Columbia, under the supervision of Dr. Gabor Forgacs. After completing his degree in 2007 he contemplates an Academic career.

He currently works as a postdoctoral associate at the Molecular and Cell Biology Department at Harvard University, in Dr. Howard Berg’s lab.

He is married to Adriana, a medical resident associated with Brown University. They have a son, Anthony.